



INSPIRING EXCELLENCE

**Influence of Li^+ Substitution on Magnetic and
Electrical Properties of $Li_xCu_{0.5}Zn_{0.5-2x}Fe_{2+x}O_4$**

Thesis submitted to

The Department of Mathematics and Natural Sciences, BRAC
University in partial fulfillment of the requirements for the award of the
Degree of Bachelor of Science in Applied Physics and Electronics

By

Anjum Mustafa

ID: 14215001

Department of Mathematics and Natural Sciences

BRAC University

Fall 2018

CANDIDATE'S DECLARATION

It is hereby declared that this Thesis titled “Influence of Li^+ Substitution on Magnetic and Electrical Properties of $Li_xCu_{0.5}Zn_{0.5-2x}Fe_{2+x}O_4$ ”, is submitted to the Department of Mathematics and Natural Sciences of BRAC University in partial fulfilment of the requirements for the degree of Bachelor of Science in Applied Physics and Electronics. This Thesis is the very own work of my own and has not been submitted elsewhere. Every work that has been used as reference has been cited properly.

Anjum Mustafa

14215001

Certified by

Dr. A.K.M Akther Hossain

Professor

Department of Physics

BUET

ACKNOWLEDGEMENTS

I firstly express all of my admiration to my parents for supporting me from the beginning of my journey.

I express my profound gratitude to my honorable supervisor **Prof. Dr. A.K.M Akhter Hossain**, Department of Physics, BUET, for his constant direction constructive criticisms and, inspiration in pursuing the whole investigation of the present research. Thanks to BUET authority for allowing me to work in the Solid State Physics Lab in BUET.

I am deeply grateful to the honorable Chairman of Department of Mathematics and Natural Sciences, **Prof. Dr. A F M Yusuf Haider** for his kind permission to let me do this work and for granting me with this opportunity.

Thanks to **Muhammad Lutfor Rahman**, honorable faculty, BRAC University for constantly coordinating my work in the entire process.

I am indebted to BRAC University for blessing me with this opportunity and providing me with enough funds to operate my research properly.

Special thanks to my co lab researcher and senior brother **Md. Zahidur Rahman**, my respected senior researcher and lab members **Rokhsana Parvin** and **Mithun Kumar Das**, without their constant help and cooperation in my work this thesis would not have been possible.

ABSTRACT

Structural, AC magnetic and electrical properties of $Li_xCu_{0.5}Zn_{0.5-2x}Fe_{2+x}O_4$ ($x=0.00$, $x=0.05$, 0.10) have been investigated which were prepared by solid state reaction method. Various chemical compositions were calcined at 800°C and samples of these compositions were sintered at 950° , 1000° , 1050° and 1100°C in air for 5 hours. The X-ray diffraction analysis, SEM (Scanning Electron Microscopy) and EDS (Energy Dispersive Spectroscopy) results were performed on the samples sintered at 1000°C . X-ray diffraction pattern confirms the formation of single phase cubic spinel structure and the lattice parameter decreases with the increase of Li^+ content obeying Vegard's law. EDS report showed the homogeneous distribution of elements in the samples. The bulk density, permeability and permittivity decreases with the Li^+ substitution. At high frequency it is found that the permeability is almost stable but the permittivity falls with the Li^+ substitution.

Table of Contents

List of Symbols and Abbreviations	8
List of Tables	9
List of Figures	10
Chapter 1	12
Introduction	12
1.1. General Introduction	12
1.2. Objectives of the Research	13
1.3. Possible Outcome of the Research	13
1.4. Summary of the Thesis	14
Chapter 2	14
Literature Review	14
2.1. Ferrites	14
2.2. Spinel Structure	15
2.3. Magnetic Moment of Electron	17
2.4. Classification of Magnetic Materials	19
2.4.1. Paramagnetism	19
2.4.2. Diamagnetism	20
2.4.3. Ferromagnetism	21
2.4.4. Antiferromagnetism	22
2.4.5. Ferrimagnetism	22
2.5. Domain Theory in Magnetism	22
2.6. Microstructure	23
2.7. Theories of Permeability	24

2.8. Mechanisms of Permeability	27
2.9. Wall Permeability	27
2.10. Rotational Permeability	29
2.11. Dielectric constant and Relative permittivity	31
Chapter 3	
Sample Preparation and Experimental Techniques	
3.1. Chemical Composition of Studied Samples	34
3.2. Various Methods for Preparing Samples	34
3.3. Solid State Reaction Method	35
3.4. Details of Calcination, Pressing and Sintering	36
3.5. Stoichiometric Ratio Calculation	39
3.6. Preparation of the Samples	41
3.7. Experimental Techniques	42
3.7.1. X-ray Diffraction	42
3.7.2. Bulk Density Measurements	43
3.7.3. Study of Microstructure	44
3.7.4. Complex Permeability Measurements	44
Chapter 4	
Results and Discussion	
4.1. X-ray Diffraction Analysis	46
4.2. Bulk Density and Porosity	48
4.3. EDS	50
4.4. Complex Initial Permeability	61
4.5. Dielectric property	66

Chapter 5	
Conclusions	68
Recommendations for Future Research	69
References	73

List of Symbols and Abbreviations

<i>AC</i> - Alternating current	<i>T_c</i> Curie temperature
<i>B</i> - Magnetic induction	<i>T_n</i> Néel temperature
(<i>θ</i>) Nelson-Riley function	<i>T_s</i> Sintering temperature
<i>f_r</i> Resonance frequency	<i>tanδ</i> Loss factor
<i>L_s</i> Self-inductance of the sample core	<i>Z</i> Complex impedance
<i>L_o</i> Inductance of the winding coil without sample	<i>μ_i</i> Initial Permeability
<i>M</i> Magnetization	<i>μ'</i> Real part of complex permeability
<i>M_s</i> Saturation magnetization	<i>μ''</i> Imaginary part of complex permeability
<i>N_A</i> Avogadro's number	<i>x-spin</i> Intrinsic rotational susceptibility
<i>P</i> Porosity	<i>x_w</i> Domain wall susceptibility
<i>P_{intra}</i> Intragranular porosity	<i>θ</i> Bragg's angle
<i>P_{inter}</i> Intergranular porosity	<i>ε_r</i> = relative permittivity
<i>Q</i> Relative quality factor	<i>ε₀</i> = permittivity of a vacuum in Farads per metre
	C= self-capacitance

LIST OF TABLES

Table 3.1: Atomic mass of the compounds	39
Table 3.2: Total molecular mass of the samples	40
Table 3.3: Calculation for the need of raw materials	40
Table 4.1: Mass of different elements in various samples of $Li_xCu_{0.5}Zn_{0.5-2x}Fe_{2+x}O_4$ sintered at $1000^\circ C$	60

List of Figures

Fig 2.1: Crystal structure of spinel ferrite	16
Fig 2.2: A and B site around an oxygen	16
Fig 2.3: Moment in a current loop	17
Fig 2.4: Electron spin and direction	18
Fig 2.5: Spin orientation of different magnetic materials in a domain	20
Fig 2.6: Domains in different field conditions	22
Fig 2.7: a) intergranular porosity, b) intragranular porosity	23
Fig 2.8: Schematic magnetization curve showing the important parameter: initial permeability, (the slope of the curve at low fields) and the main magnetization mechanism in each magnetization range	25
Fig 2.9: Magnetization by wall motion and spin rotation	27
Fig 3.1: Flow chart of the stages in preparation of spinel ferrite	36
Fig 3.2: Schematic representation of sintering stages: (a) green body, (b) initial stage, (c) intermediate stage, and (d) final stage	37
Fig 4.1: X-ray diffraction patterns for $Li_xCu_{0.5}Zn_{0.5-2x}Fe_{2+x}O_4$	46
Fig 4.2: The variation of lattice parameter with Li for $Li_xCu_{0.5}Zn_{0.5-2x}Fe_{2+x}O_4$	46
Fig 4.3: The variation of (a) bulk and theoretical density sintered at 1100° C and (b) Bulk density versus porosity	48
Fig 4.4: EDS pattern at point 1 for x=0.00	50
Fig 4.5: EDS pattern at point 2 for x=0.00	51
Fig 4.6: EDS pattern at point 3 for x=0.00	52
Fig 4.7: EDS pattern at point 1 for x=0.05	53
Fig 4.8: EDS pattern at point 2 for x=0.05	55
Fig 4.9: EDS pattern at point 3 for x=0.05	56

Fig 4.10: EDS pattern at point 1 for x=0.10	56
Fig 4.11: EDS pattern at point 2 for x=0.10	57
Fig 4.12: EDS pattern at point 3 for x=0.10	58
Fig 4.13. The real and imaginary part of permeability spectrum for $Li_xCu_{0.5}Zn_{0.5-2x}Fe_{2+x}O_4$ sintered at 950° C in the air	61
Fig 4.14: The real and imaginary part of permeability spectrum for $Li_xCu_{0.5}Zn_{0.5-2x}Fe_{2+x}O_4$ sintered at 1000° C in the air	61
Fig 4.15: The real and imaginary part of permeability spectrum for $Li_xCu_{0.5}Zn_{0.5-2x}Fe_{2+x}O_4$ sintered at 1050° C in the air	62
Fig 4.16: The real and imaginary part of permeability spectrum for $Li_xCu_{0.5}Zn_{0.5-2x}Fe_{2+x}O_4$ sintered at 1100° C in the air	62
Fig 4.17: Relative Quality Factor at 950°C	63
Fig 4.18: Relative Quality Factor at 1000°C	63
Fig 4.19: Relative Quality Factor at 1050°C	63
Fig 4.20: Relative Quality Factor at 1100°C	63
Fig 4.21: For x=0.00, at various temperature: a) permeability b) RQF	64
Fig 4.22: For x=0.05, at various temperature: a) permeability b) RQF	64
Fig 4.23: For x=0.10, at various temperature: a) permeability b) RQF	65
Fig 4.24: At 1000° C: a) permittivity b) dielectric loss	66
Fig 4.25: At 1050° C: a) permittivity b) dielectric loss	66

CHAPTER 1

Introduction

1.1. General Introduction

Polycrystalline spinel type ferrites are very important material due to their numerous applications in various fields. They play an important role in plenty of applications in many electronic devices. Many significant characteristics made ferrite a superior material such as high permeability and saturation magnetization in the radio frequency region, high electrical resistivity, mechanical hardness and chemical stability [1]. They are also used to stop RF interference to audio systems. Not to mention that their AB_2O_4 structure can create various magnetic properties according to cation doping and substitution [2].

In microwave application Lithium ferrite and mixed lithium ferrite has significant role. More specifically as replacement of garnets because of their low costs [3]. Moreover Lithium ferrites has high resistivity, low dielectric loss, high temperature and square hysteresis loop properties which makes it an important and significant material among the others. Therefore lithium ferrites are used as microwave devices like circulators, isolators and phase shifters [26].

Lithium ferrite can be prepared in various methods such as high energy ball milling, sol gel technique, micellar reactions, sucrose method, coprecipitation, solid state reaction method and combustion synthesis. Altering the substitution with metal ions like cobalt (Co^{2+}), Nickel (Ni^{2+}), Zirconium (Zr^{2+}), Zinc (Zn^{2+}), titanium etc. various experiment can be performed [26].

In this experiment we established Zinc substituted Li-Cu ferrite polycrystalline synthesis by solid state reaction method. The structural properties of ferrite have been explored by XRD, magnetic and Dielectric properties are measured by impedance analyzer [3].

1.2. Objective of the Research

Particular ferrite material can be used in many electronic devices due to their high permeability and stability in high frequency range. Ferrite has high resistivity, low eddy current and power loss. Moreover ferrites are good filters, it reduces unwanted high frequency electrical disturbance. Therefore by investigating the properties of ferrite and finding appropriate material for industrial use and application in practical life is the main objective of this research. Work procedure of this research includes:

- (a) Preparation samples of $Li_xCu_{0.5}Zn_{0.5-2x}Fe_{2+x}O_4$ in solid state reaction method for $x= 0.00, x=0.05$ and 0.10
- (b) Perform structural characterizations (x-ray diffraction), density and porosity.
- (c) Complex permeability as a function of frequency (100KHz - 120MHz)
- (d) Investigation of surface morphology

1.3. Possible Outcome of the Research

As the calculated Bohr magneton was high it is expected that the permeability of the samples will increase and the material will be more stable in high frequency. Moreover due to Li^+ substitution it is expected that the sample might have some electrical properties as well.

1.4. Summary of the Thesis

Summary of the thesis is as follows:

Chapter 1- Introduction and objective of the research

Chapter 2- Provides basic information on ferrites, their structures and permeability mechanism

Chapter 3- Details of sample preparation and experimental techniques

Chapter 4- Includes results and discussion

Chapter 5- Conclusions and recommendations for future research.

CHAPTER 2

Literature Review

2.1. Ferrites

Ferrites are ceramic type materials with magnetic properties consisting of mixture of various metal oxides usually includes iron oxides and one or more other metals, which are useful in many types of electronic devices. Ferrites are electrically non-conductive ferromagnetic ceramics. They are usually mixture of iron oxides, such as hematite (Fe_2O_3), Magnetite (Fe_3O_4) and oxides of other metals. They are hard and brittle.

General chemical formula of ferrite is AB_2O_4 where A and B represent different metal cations [4].

They are hard, brittle, iron containing, polycrystalline and ferrimagnetic. Saturation magnetization, high electrical resistivity, low electrical losses, and chemical stability-such characteristics make ferrite a demandable material. The general formula of ferrite is $MeO.Fe_2O_3$ where Me is any metals (Ni, Cu, Zn, Mn, Mg, etc.) that forms divalent ions. Many scientists have come up with a lot of investigation on ferrites and their properties. Snoek's work particularly focuses on the high permeability of ferrites that was a combination of different metals with ferric oxides in the form of $MeZnFe_2O_4$ [5]. His work is one of the oldest researches on ferrites. Current researches include the study of La^{3+} substitution on structure, surface morphology and magnetic properties of Ni-Zn ferrite, synthesis of pure and mixed nickel-cobalt ferrite, investigation on structural, dielectric and electrical properties of Zn substituted Li-Ni ferrite [6,7-8].

2.2. Spinel Structure

Ferrite has spinel structure similar to the mineral spinel of $MgO.Al_2O_3$ which is also known as cubic spinel. Spinel structure is usually consists of cubic close packed oxides with two tetrahedral and four octahedral sites per unit formula and has formula of $AO.B_2O_3$ or AB_2O_4

where A and B [9] represent the divalent metal (A^{2+}) and the trivalent (B^{3+}) cations respectively [9]. All A^{2+} ions occupy the tetrahedral sites and all B^{3+} ions occupy the octahedral sites. In fig 2.1 a simple spinel structure is given of the mineral spinel magnesium-aluminum. Considering a single unit of the spinel, A site is shown in the middle surrounded by four oxygen atoms in a tetrahedral structure, and B site is surrounded by 6 neighboring oxygen neighbors who form an octahedral site. Thus the total structure is a repeating array of the lattices containing two tetrahedral and four octahedral sites. In total a single unit consists of eight sub cells with 8 A sites, 16 B sites, and 32 oxygen ions. In figure 2(b) a tetrahedral and octahedral structure of are shown. When chemical bonding happens, metal ions enter the A site. The void in between the oxygen ions play an important role whether to accommodate a bigger or smaller ion. If the size of the ion is bigger than the size of the intermolecular distance between two oxygens then it may possible that metal ions may not occupy the A site properly. As the oxygen ions are closely packed together, the metal ions often move the oxygen ions slightly to make rooms for their own. These oxygen ions push the surrounding octahedral sites the same amount. As a result while the tetrahedral site expands, the size of the octahedral site lessens.

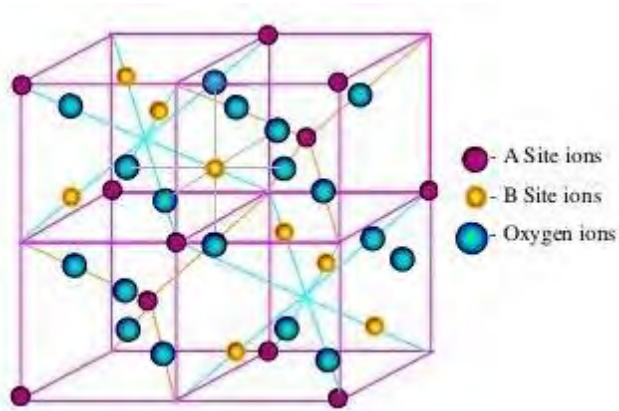


Fig 2.1: Crystal structure of spinel ferrite

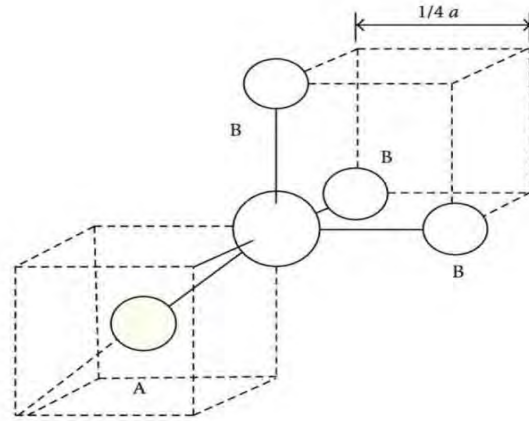


Fig 2.2: A and B site around an oxygen

2.3. Magnetic Moment of Electron

All sorts of materials have magnetic moments according to their alignment of electron spins. If an object is placed in an external magnetic field, it feels a torque to align its spins in the direction of the external magnetic field. Magnetic moment is the quantity that indicates the torque for which the object tends to produce its own magnetic field. Starting from a tiny electron to a huge planet—all has magnetic fields. Especially in the case of electron spin ‘magnetic moment’ is used instead of magnetic field that has both magnitude and direction. It can be compared to a current loop. When current flows in a wire loop, it produces magnetic field and the direction the magnetic field depends on the direction of the current flow. (Right hand rule). The magnetic moment (μ_c) of the loop is

$$\mu_c = I \int dS \quad (2.1)$$

Where, I = Current in the loop (A) ; S = Surface area (m^2)

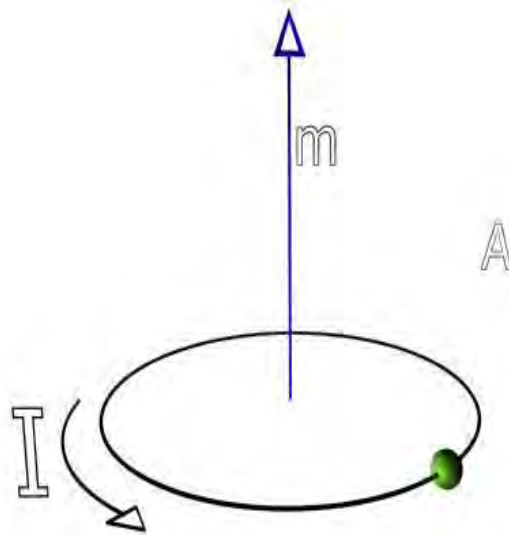


Fig 2.3: Moment in a current loop

We know current is nothing but flow of electrons. Let's consider two electrons in an orbital. Their magnetic dipole moment is caused by the rotation and electric charge which is given by

$$\mu_B = \frac{e\hbar}{2me}$$

μ_B is known as Bohr magneton.

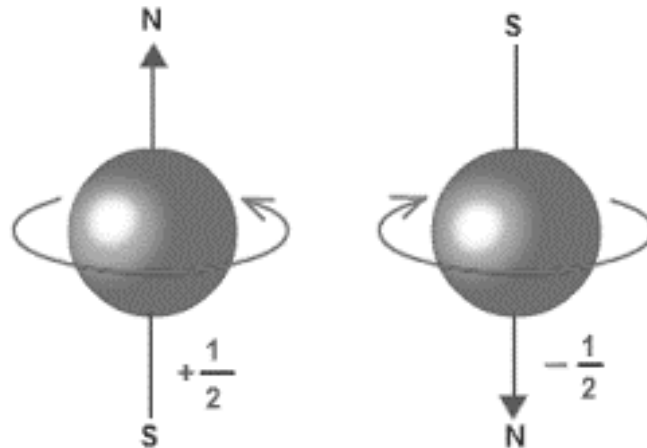


Fig 2.4: Electron spin and direction

Figure 2(d) represents a system of two electrons that both have a spin of half but in different direction. Due to the opposite direction the electrons produce magnetic fields just like the current loop having same magnitude but in the opposite direction, one electron eliminates the other one, nullifying the total magnetic field into zero.

2.4. Classification of Magnetic Materials

When a material is placed in an external magnetic field, it feels a torque that tries to bend, distort or rearrange its electron spin configuration. This effect is known as Faraday's law of induction. This effect along with a number of other factors like atomic and molecular structure of the material, paired or unpaired electrons play a crucial role on how a material will behave and how their spins will be arranged in which manner if they are placed in a magnetic field. Depending on the spin orientation magnetic materials have been divided into five major groups. Each group represents special configuration of electron spins and therefore, show different magnetic properties.

2.4.1. Paramagnetism

These substances are poorly magnetized by an external field in the same direction of the applied field. Although they are attracted toward magnets, however they also lose their magnetic attributes once the field is removed. Unlike diamagnetic materials they have permanent magnetic moments due to some unpaired electrons in partially filled orbitals. These moments interact with each other weakly and randomly orient in different directions. That gives a very small net magnetic moment and a very small but positive value of susceptibility. Chromium, aluminum,

alkali and alkaline earth metals are some known paramagnetic materials. Their susceptibility (X) is inversely proportional to temperature (T) and follow the Curie-Weiss law,

$$X = \frac{C}{T - \theta} \quad (2.3)$$

where,

C is the curie constant

θ is a specific temperature for magnetic materials

For paramagnetic case, θ is zero [10].

It means when the temperature increases, it becomes harder to hold the spin alignment in the same direction. The thermal agitation becomes more impulsive to destroy the spin orientation completely.

2.4.2. Diamagnetism

Diamagnetic materials are those who have a nature to be magnetized very weakly by an applied magnetic field but in the opposite direction. They are repelled by the magnetic field and do not retain magnetic properties once the field is removed. For example, bismuth, antimony, water, alcohol, argon, copper, mercury, gold, tincture are diamagnetic materials. Diamagnetic materials have this wonderful feature to levitate in air to resist the field that is imposed on them. They have all paired electrons per atom for which the entire magnetic moment of the material is zero, therefore, show no tendency to be attracted by even a powerful magnet. On the contrary, they are repelled as they induce dipole moments in such way that it works in the opposite direction. Another property of the material is that they are independent of temperature [11] and have the negative magnetic susceptibility, given by

$$X = \mu_r - 1 \quad (2.4)$$

Where susceptibility X is in between the order of -10^{-6} to -10^{-5} . Figure 2(e) shows the spin orientation of magnetic materials in the absence and presence of external magnetic field.

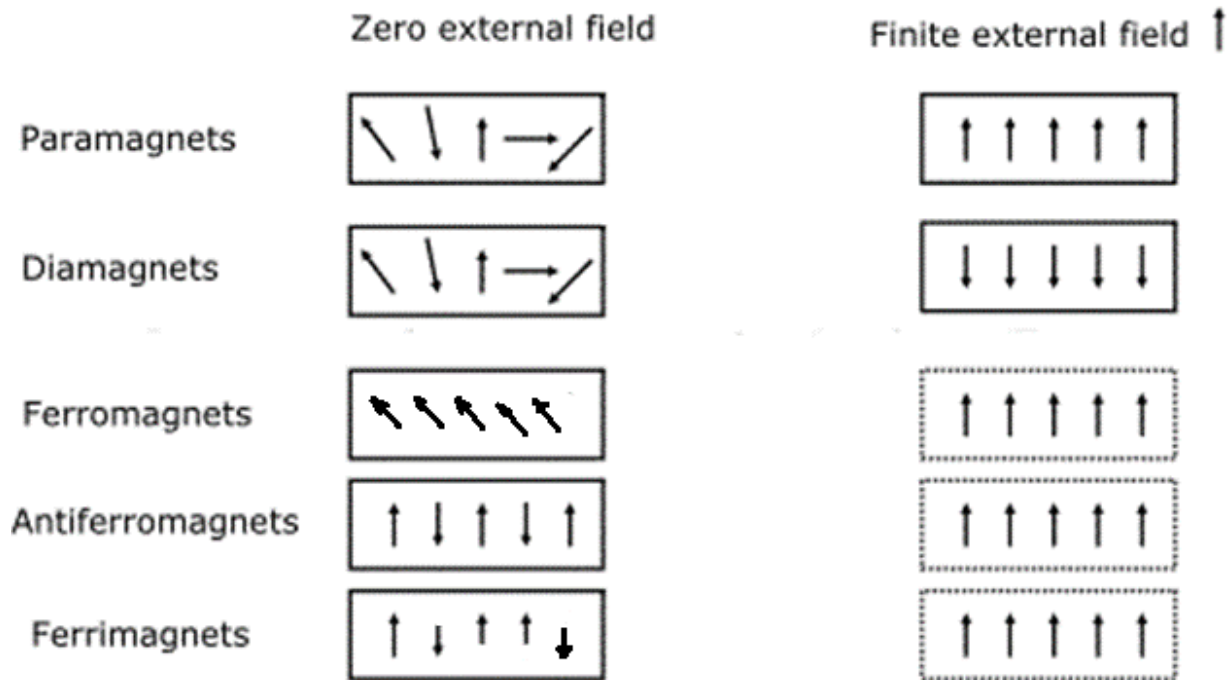


Fig 2.5: Spin orientation of different magnetic materials in a domain

2.4.3. Ferromagnetism

Ferromagnets are easily magnetized by the application of magnetic field. They tend to align their spins in the direction of the magnetic field and have this unique feature of retaining the magnetic properties even after the field is removed. They have unpaired electrons in orbitals that interacts with each other strongly and such atomic structure supports them to align their spin in the same direction of the magnetic field. They are used to make permanent magnets. They get their strong magnetic behavior because of the magnetic domains. In these domains, spins are aligned in the same direction within the domains to gain a large amount of magnetic moments so that the moment of individual domain is strong, but the net moment of all the domains is zero [11]. They have high permeability in the order of 10^3 to 10^5 and high susceptibility (way more than diamagnetic and paramagnetic) that varies along with temperature. All ferromagnets have a maximum temperature above which they lose their spin orientation because of thermal agitation. It is known as the Curie temperature when achieved, the ferromagnets lose their magnetic abilities.

2.4.4. Antiferromagnetism

Antiferromagnetic materials are those who have anti parallel alignment of electron spins between neighboring electrons to cancel each other's moments much like the paramagnetic materials. The only element that shows this kind of behavior is chromium in the room temperature. Antiferromagnetic materials own a specific temperature called Neel temperature above which their antiferromagnetism property disappears.

2.4.5. Ferrimagnetism

Ferrimagnetism belong to a group of compounds those having exchange interactions leading to parallel alignments of atoms in some sights and anti-parallel alignments of atoms in some sights [12]. They have similarities with ferromagnetic materials having lower saturation magnetizations. Ferrimagnetism has characteristics like spontaneous magnetization like ferromagnets and above Curie temperature they have zero magnetic order like paramagnets. They have high resistivity and anisotropy which are proving to be very useful in the technological applications.

2.5. Domain Theory in Magnetism

The domain theory explains why ferromagnets can retain their properties even after removing magnetic field. Ferromagnets are divided into some very small region that own a group electrons having the same direction within the same domain. These domains are about 10^{-12} to $10^{-8} m^3$ in size. The interaction within one domain is so strong that they produce a net moment although it gets cancelled by the moment which is created by another domain. Ferromagnets contain millions of domain like these making the total magnetic flux zero. When a strong magnetic field is applied, the spin directions of all domain get aligned producing a humongous net magnetic flux that tries to keep the alignment same even after removing the field, however, the alignment may shift a little which is shown by the figure below. This result is explained by the hysteresis curve, why ferromagnets do not follow the same path of magnetization with increasing and decreasing of magnetic field which is known as the remnant magnetization.

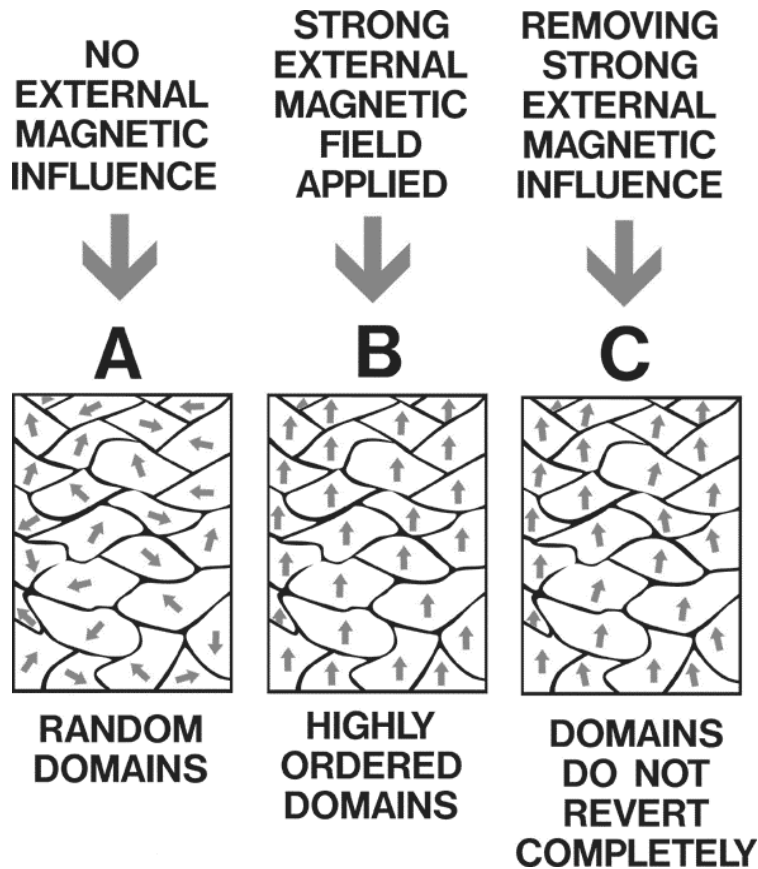


Fig 2.6: Domains in different field conditions

2.6. Microstructure

Microstructure is basically the arrangements of phases and defects within a material in nm length scale obtained using microscope. Microstructure are formed when a material under goes by phase transition through sintering or pressurizing, deforming etc. Microstructure study is pivotal in ferrite composition because to a great extent, the physical properties of the material is driven by microstructure or more specifically the grain boundaries. Grain boundary is the region of interface between two grains of the same phase in a polycrystalline material. Grains are formed of atoms that share lose bonds with each other within that grain. When stress is applied, the bond between the atoms are pulled apart forming dislocations gradually appearing as grain boundary.

Porosity, a common term that appears with microstructure of crystallography, it is the void or empty space in a crystal structure. There are two types of porosity seen in grain size.

a) Intergranular and b) Intragranular porosity. Intragranular occurs within a grain and intergranular occurs in between grains.

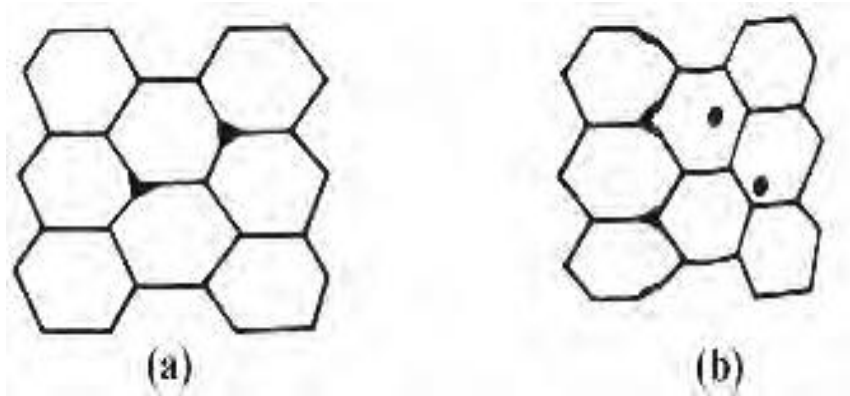


Fig 2.7: a) intergranular porosity, b) intragranular porosity

2.7. Theories of Permeability

One of the primary objectives of studying ferrites is to obtain such material composition that has high permeability with low loss. Permeability indicates the degree of magnetization or magnetic field induction B of a material in an applied field intensity H [13, 14]. Permeability is given by,

$$B = \mu H \quad (2.5)$$

μ is the proportional constant between the induced and applied field.

If the applied field is very low, approaching to zero, the ratio then called the initial permeability and written as,

$$\mu_i = \frac{\Delta B}{\Delta H_{(\Delta H \rightarrow 0)}} \quad (2.6)$$

If a magnetic field is subjected to an AC magnetic material, we get

$$B = B_0 e^{i\omega t} \quad (2.7)$$

It is observed that the magnetic flux density B experiences a delay which is caused due to the presence of various losses and is thus expressed as,

$$B = B_0 e^{i(\omega t - \delta)} \quad (2.8)$$

Where, δ is the phase angle and indicates the delay of B with respect to H . The permeability is then given by

$$\mu = \frac{B}{H} = \frac{B_0 e^{i(\omega t - \delta)}}{H_0 e^{i\omega t}} = \frac{B_0 e^{-i\delta}}{H_0} = \frac{B_0}{H_0} \cos \delta - i \frac{B_0}{H_0} \sin \delta = \mu' - i\mu''$$

Where,

$$\mu' = \frac{B_0}{H_0} \cos \delta \quad (2.9)$$

and

$$\mu'' = \frac{B_0}{H_0} \sin \delta \quad (2.10)$$

The real part (μ') of the complex initial permeability represents the component of B that is in phase with H , so it corresponds to the normal permeability. If there are no losses we should get $\mu = \mu'$. The imaginary part (μ'') is the component that lags behind H by the phase angle. The presence of such a component requires supply of energy to maintain the alternating magnetization, regardless of the origin of delay. It is useful to introduce the loss factor $\tan \delta$ the ratio of μ'' to μ' which can be obtained by,

$$\frac{\mu''}{\mu'} = \frac{\frac{B_0}{H_0} \sin \delta}{\frac{B_0}{H_0} \cos \delta} = \tan \delta \quad (2.11)$$

This $\tan \delta$ is called loss factor.

The quality factor is defined as the reciprocal of this loss factor, i.e.

$$\text{Quality factor} = \frac{1}{\tan \delta} \quad (2.12)$$

And the relative quality factor,

$$Q = \frac{\mu'}{\tan \delta}$$

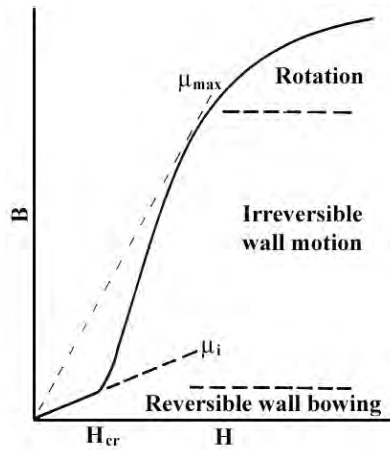


Fig 2.8: Schematic magnetization curve showing the important parameter: initial permeability, μ_i (the slope of the curve at low fields) and the main magnetization mechanism in each magnetization range.

The graph illustrates the behavior of both μ' and μ'' with frequency are called the complex permeability spectrum of the material [15]. The measurement of complex permeability gives us valuable information about the nature of domain wall and their movements. In dynamic measurements the eddy current loss is very important that occurs due to the irreversible domain wall movements. The permeability of a ferrimagnetic substance is the combined effect of the wall permeability and rotational permeability mechanisms.

2.8. Mechanism of Permeability

The mechanisms can be explained as follows: A demagnetized magnetic material is divided into number of Weiss domains separated by Bloch walls. In each domain all the magnetic moments are oriented in parallel and the magnetization has its saturation value M_s . In the walls the magnetization direction changes gradually from the direction of magnetization in one domain to that in the next. The equilibrium positions of the walls result from the interactions with the magnetization in neighboring domains and from the influence of pores; crystal boundaries and chemical inhomogeneities which tend to favor certain wall positions.

2.9. Wall Permeability

The mechanism of wall permeability arises from the displacement of the domain walls in small fields. Let us consider a piece of material in the demagnetized state, divided into Weiss domains with equal thickness L by means of 180° Bloch walls as shown in figure 2.9. The walls are parallel to the YZ plane. The magnetization M_s in the domains is oriented alternately in the $+Z$ or $-Z$ direction. When a field H with a component in the $+Z$ direction is applied, the magnetization in this direction will be favored. A displacement dx of the walls in the direction shown by the dotted lines will decrease the energy density by an amount [16, 17]:

$$\frac{2M_s H_z dx}{L}$$

This can be described as a pressure $M_s H_z$ exerted on each wall. The pressure will be counteracted by restoring forces which for small deviations may assume to be kdx per unit wall surface. The new equilibrium position is then given by

$$d = \frac{M_s H_z dx}{L}$$

From the change in the magnetization

$$\Delta M = \frac{2M_s d}{L},$$

The wall susceptibility χ_w may be calculated. Let H makes the angle θ with Z direction. The magnetization in the θ direction becomes

$$(\Delta M)_\theta = \frac{2M_s d}{L} \cos \theta, \text{ And with } H_z = H \cos \theta \text{ and } d = \frac{2M_s H_z}{K}$$

We obtain

$$\chi_w = \frac{(\Delta M)_\theta}{H} = \frac{4M_s^2 \cos^2 \theta}{KL}$$

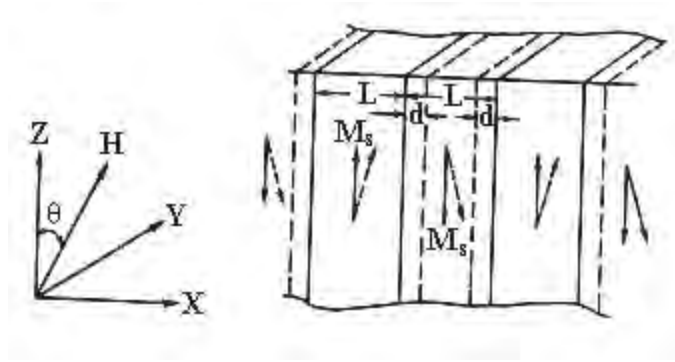


Fig 2.9: Magnetization by wall motion and spin rotation.

2.10. Rotational Permeability

The rotational permeability mechanism arises from rotation of the magnetization in each domain. The direction of M can be found by minimizing the magnetic energy E as a function of the orientation. Major contribution to E comes from the crystal anisotropy energy. Other contributions may be due to the stress and shape anisotropy. The stress may influence the magnetic energy via the magnetostriction. The shape anisotropy is caused by the boundaries of the sample as well as by pores, nonmagnetic inclusions and inhomogeneities. For small angular deviations, α_x and α_y may be written as

$$\alpha_x = \frac{M_x}{M_s} \text{ and } \alpha_y = \frac{M_y}{M_s} .$$

For equilibrium Z - direction, E may be expressed as [18, 19]

$$E = E_0 + \frac{1}{2} \alpha_x^2 E_{xx} + \frac{1}{2} \alpha_y^2 E_{yy}$$

Where it is assumed that x and y are the principal axes of the energy minimum. Instead of E_{xx} & E_{yy} , the anisotropy field H_x^A and H_y^A are often introduced. Their magnitude is given by

$$H_x^A = \frac{E_{xx}}{2M_s} \text{ and } H_y^A = \frac{E_{yy}}{2M_s}$$

H_x^A & H_y^A represent the stiffness with which the magnetization is bound to the equilibrium direction for deviations in x and y direction, respectively. The rotational susceptibilities $\chi_{r,x}$ and $\chi_{r,y}$ for fields applied along x and y directions, respectively are

$$\chi_{r,x} = \frac{M_s}{H_x^A} \text{ and } \chi_{r,y} = \frac{M_s}{H_y^A}.$$

For cubic materials it is often found that H_x^A and H_y^A are equal. For $H_x^A = H_y^A = H^A$ and a field H which makes an angle θ with the Z direction the rotational susceptibility, $\chi_{r,c}$ in one crystallite becomes

$$\chi_{r,c} = \frac{M_s}{H^A} \sin^2 \theta$$

A polycrystalline material consisting of a large number of randomly oriented grains of different shapes, with each grain divided into domains in a certain way. The rotational susceptibility χ_r of the material has to be obtained as a weighted average of $\chi_{r,c}$ of each crystallite, where the mutual influence of neighboring crystallites has to be taken into account. If the crystal anisotropy dominates other anisotropies, then H^A will be constant throughout the material, so only the factor $\sin^2 \theta$ has to be averaged. Snoek [19] assuming a linear averaging of $\chi_{r,c}$ and found

$$\chi_r = \frac{2M_s}{3H^A}$$

The total internal susceptibility

$$\chi = \chi_w + \chi_r = \frac{4M_s^2 \cos^2 \theta}{KL} + \frac{2M_s}{3H^A}$$

If the shape and stress anisotropies cannot be neglected, H^A will be larger. Any estimate of χ_r will then be rather uncertain as long as the domain structure, and the pore distribution in the material are not known. A similar estimate of χ_w would require knowledge of the stiffness parameter k and the domain width L . These parameters are influenced by such factors as imperfection, porosity and crystallite shape and distribution which are essentially unknown.

2.11. Dielectric Constant & Relative Permittivity

- **Absolute permittivity:** Absolute permittivity is defined as the measure of permittivity in a vacuum and it is how much resistance is encountered when forming an electric field in a vacuum. The absolute permittivity is normally symbolized by ϵ_0 . The permittivity of free space - a vacuum - is equal to approximately 8.85×10^{-12} Farads / meter (F/m)
- **Relative permittivity:** Relative permittivity is defined as the permittivity of a given material relative to that of the permittivity of a vacuum. It is normally symbolized by: ϵ_r .
- **Static permittivity:** The static permittivity of a material is defined as its permittivity when exposed to a static electric field. Often a low frequency limit is placed on the

material for this measurement. A static permittivity is often required because the response of a material is a complex relationship related to the frequency of the applied voltage.

- ***Dielectric constant:*** The dielectric constant is defined as the relative permittivity for a substance or material [30].

The relative permittivity of a material is its (absolute) permittivity expressed as a ratio relative to the permittivity of vacuum.

Permittivity is a material property that affects the Coulomb force between two point charges in the material. Relative permittivity is the factor by which the electric field between the charges is decreased relative to vacuum.

Likewise, relative permittivity is the ratio of the capacitance of a capacitor using that material as a dielectric, compared with a similar capacitor that has vacuum as its dielectric. Relative permittivity is also commonly known as dielectric constant, a term deprecated in engineering as well as in chemistry

Relative permittivity is typically denoted as $\epsilon_r(\omega)$ (sometimes κ or K) and is defined as

$$\epsilon_r(\omega) = \frac{\epsilon(\omega)}{\epsilon_0}$$

where $\epsilon(\omega)$ is the complex frequency-dependent absolute permittivity of the material, and ϵ_0 is the vacuum permittivity.

The relative static permittivity, ϵ_r , can be measured for static electric fields as follows: first the capacitance of a test capacitor, C_0 , is measured with vacuum between its plates. Then, using the same capacitor and distance between its plates, the capacitance C with a dielectric between the plates is measured. The relative permittivity can be then calculated as

For time-variant electromagnetic fields, this quantity becomes frequency-dependent. An indirect technique to calculate ϵ_r is conversion of radio frequency S-parameter measurement results. A description of frequently used S-parameter conversions for determination of the frequency-dependent ϵ_r of dielectrics can be found in this bibliographic source. Alternatively, resonance based effects may be employed at fixed frequencies[31].

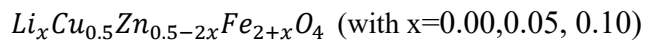
CHAPTER 3

Sample Preparation and Experimental Techniques

This chapter provides an overview of the sample preparation and methods that have been used to determine different parameters of the ferrites.

3.1. Chemical Composition of Studied Samples

In this present work, the compositions of Li^+ doped $Li_xCu_{0.5}Zn_{0.5-2x}Fe_{2+x}O_4$ were synthesized and investigated. The samples were:



3.2. Various Methods for Preparing Samples

There are a number of methods which are followed to study ferrites and their compositions. Among these, the conventional ceramic process and solid state reaction method are widely used to prepare ferrite powder. Other methods are [20, 21],

- 1) Sol-gel synthesis
- 2) Co-precipitation
- 3) Organic precursors
- 4) Freeze drying
- 5) Spray drying
- 6) Combustion synthesis

7) Glass crystallization

For this experiment, solid state method reaction method is used which is described thoroughly below

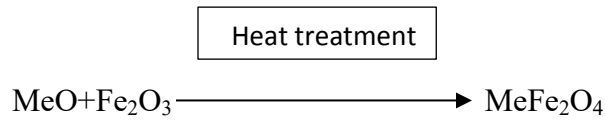
3.3. Solid State Reaction Method

Solid state reaction method consists of several steps to get the final products which are been studied. Solids do not react at room temperature over normal time scales for which it is necessary to heat them at higher temperature to complete chemical reaction. This reaction depends on factors such as structural properties of the reactants, surface area of the solids, reactions conditions and their thermodynamics [20].

The required composition is usually prepared from the appropriate amount of raw materials of oxides or carbonates by crushing, grinding and milling.

Once the powders are finely ground, they are calcined in air for 5 hours at temperature above 500°C . Calcine temperature may vary according to needs. The calcination process makes the impurities go away. The calcined powders are then again hand milled to ensure they are properly smoothed. The necessary pellets and toroid samples are prepared from the calcined powder according to the need using die punch assembly or hydrostatic or isostatic pressure. Sintering is carried out at temperatures from 950°C to 1150°C for a typical time of 1 to 10 hours in different atmospheres [22, 23].

The general solid state reaction leading to a ferrite MeFe_2O_4 may be represented as



Where Me is the metal ions. There are basically four steps in the preparation of ferrites.

- 1) Preparation of materials to form an intimate mixture with the metal ions in the ratio which they will have in the final product.
- 2) Calcining the mixture to form ferrite.
- 3) Grinding the calcined powders and pressing to get the required shape.
- 4) Sintering to produce highly densified product.

3.4. Details of Calcination, Pressing and Sintering

Calcination is a process of obtaining a homogenous and phase pure composition of mixed powders by heating them for a certain amount of time at a certain temperature and then cooled down slowly. Calcination can be repeated several times to obtain a high degree of homogeneity. The calcined powders are then again crushed.

A binder is usually added prior to compaction at a concentration lower than 5wt%. Binders are polymers or waxes that are used to facilitate the particles flow during compacting and increase the bonding between particles. The most commonly used binder for ferrites is polyvinyl acid. During sintering binders decompose and are eliminated from the ferrite. Pressures are used to for compacting very widely but are commonly several tons per square inch. (i.e. up to 10^8 nm^{-2}) to desired toroid and pellet shapes.

Sintering process makes a sample more dense, tough body by heating a compacted powder for a certain period of time at high temperature enough to promote diffusion but surely below the melting point of the main component.

Below is given the process of sample preparation through by a flowchart:

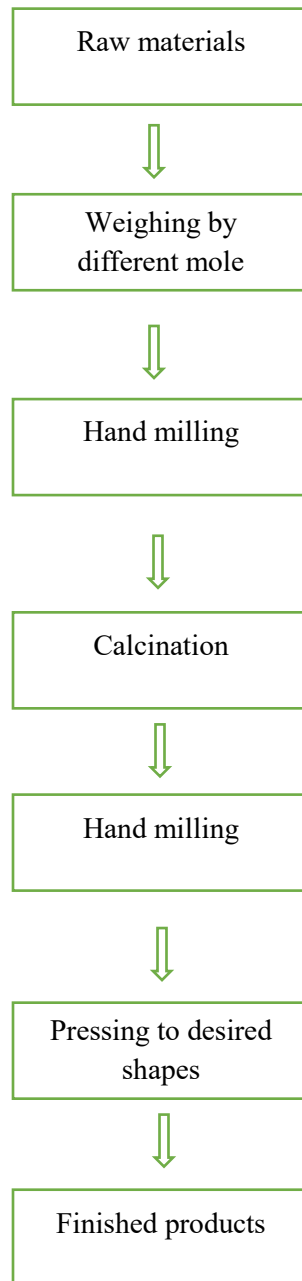


Fig 3.1: Flow chart of the stages in preparation of spinel ferrite

The purposes of sintering process are-

- 1) To bind the particles to impart sufficient strength to the product.
- 2) To densify the material and eliminating pores.
- 3) Gain homogeneity by completing the reactions left unfinished in calcination.

Coble and burke [23] found out the empirical relation regarding rate of grain growth which is given by

$$d = \bar{k}t^n \quad (3.1)$$

Where \bar{d} is the mean grain diameter. n is about $1/3$, t is the sintering time and k is a temperature dependent parameter. Sintering is divide into 3 stages [23, 24],

- 1) Contact area between particle increases.
- 2) Porosity changes from open to close porosity
- 3) Pore volume decreases and gains grow.

The following figure shows the grain growth at different sintering stages.

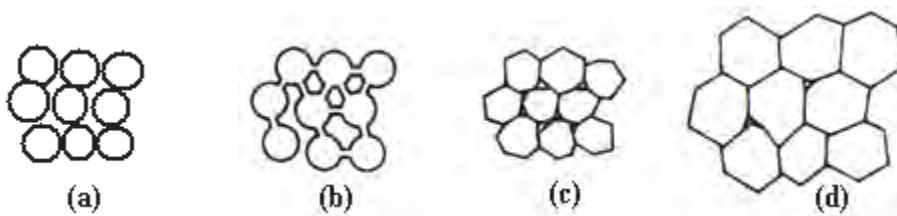


Fig 3.2: Schematic representation of sintering stages: (a) green body, (b) initial stage, (c) intermediate stage, and (d) final stage

3.5. Stoichiometric Ratio Calculation

The following tables show the calculation of different amount of raw materials that was taken to make the samples. For the samples used in this work, each was of a total of 15 gram and each pellet and ring were made of 1 gram.

Table 3.1: Atomic mass of the compounds

Raw materials	Li (g/mole)	Cu (g/mole)	Zn (g/mole)	C (g/mole)	Fe (g/mole)	O (g/mole)	Total (g/mole)
Li_2CO_3	6.941			12.0107		15.999	73.89
Cu_2O		63.546				15.999	143.08
ZnO			65.38			15.999	81.37
Fe_2O_3					55.85	15.999	159.69

Table 3.2: Total mass of the sample

Value of x	Composition	Mass of the sample (g/mole)
0.00	$Cu_{0.5}Zn_{0.5}Fe_2O_4$	$(63.546*0.5)+(65.38*0.5)+(55.85*2)+(15.999*4)$ = 240.1506
0.05	$Li_{0.05}Cu_{0.5}Zn_{0.4}Fe_{2.05}O_4$	$(6.941*0.05)+(63.546*0.5)+65.38*0.4+(55.85*2.05)$ + $(15.999*4)$ = 236.7519
0.10	$Li_{0.10}Cu_{0.5}Zn_{0.3}Fe_{2.10}O_4$	$(6.941*0.10)+ (63.546*0.5)+(65.38*0.3)$ + $(55.85*2.10)+(15.999*4)$ = 233.7519

Table 3.3: Calculation for the need of raw materials

Composition	Need of	Amount (g/mole)
$Cu_{0.5}Zn_{0.5}Fe_2O_4$	Li_2CO_3	0

$Cu_{0.5}Zn_{0.5}Fe_2O_4$	Cu_2O	$(143.08*0.5*15)/(240.1506*2)=2.2342$
	ZnO	$(81.37*0.5*15)/240.1506=2.5412$
	Fe_2O_3	$(159.69*15*2)/(240.1506*2)=9.9744$
$Li_{0.05}Cu_{0.5}Zn_{0.4}Fe_{2.05}O_4$	Li_2CO_3	$(73.89*0.05*15)/(236.7519*2)= 0.1170$
	Cu_2O	$(143.08*0.5*15)/(236.7519*2)= 2.2663$
	ZnO	$(81.37*0.4*15)/236.7519=2.0622$
	Fe_2O_3	$(159.69*2.05*15)/(236.7519*2)=10.3704$
$Li_{0.10}Cu_{0.5}Zn_{0.3}Fe_{2.10}O_4$	Li_2CO_3	$(73.89*0.10*15)/(233.3532*2)=0.2375$
	Cu_2O	$(143.08*0.5*15)/(233.3532*2)=2.2993$
	ZnO	$(81.37*0.3*15)/233.3532=1.5691$
	Fe_2O_3	$(159.69*2.10*15)/(233.3532*2)=10.7782$

3.6. Preparation of the Sample

$Li_xCu_{0.5}Zn_{0.5-2x}Fe_{2+x}O_4$ (with $x=0.00, 0.05, 0.10$) were prepared by solid state reaction method with the stoichiometric amount of raw materials. The extra pure powder (99.9%) of Li_2CO_3 , Cu_2O , ZnO , Fe_2O_3 are weighted according to the required composition and hand milled for about 5 hours for chemical reaction to happen using an agitate mortar and pistol. Before using mortar and pistol, they were cleaned each and every time very carefully to avoid impurity

mixing. This is facilitated further by calcination which is undertaken for 5 hours in air at a temperature of 950⁰ C. The calcined powders were granulated using polyvinyl acid a binder and pressed in to desired toroid and pellet shapes. In the final stage they were sintered at various temperatures from 950⁰ to 1100⁰ C in air for 5 hours. The temperature ramps for sintering are 5⁰C /min for heating and 10⁰C /min for cooling.

3.7. Experimental Techniques

In this chapter, the basic experimental techniques of measuring lattice parameter and frequency depended permeability of ferrite sample is described.

3.7.1. X-ray Diffraction

If a monochromatic radiation of wavelength λ is incident on periodic crystal plane at an angle of θ and is diffracted at the same angle as shown in the figure, the Bragg diffraction condition is given by

$$2d \sin \theta = n\lambda \quad (3.2)$$

Where d is the distance between crystal planes and n is the positive integer which represents the order of reflection. Equation (4.1) is known as Bragg law. This Bragg law suggests that the diffraction is only possible when $\lambda \leq 2d$. The X-ray diffraction provides substantial information of the crystal structure.

Pellets of $Li_xCu_{0.5}Zn_{0.5-2x}Fe_{2+x}O_4$ (with $x=0.00, 0.05, 0.10$) sintered at 1000^o is used for X-ray diffraction. The lattice parameter for each peak of each sample is calculated by the formula given below,

$$a = d \sqrt{h^2 + k^2 + l^2} \quad (3.3)$$

Where h , k and l are the indices of the crystal planes. To determine the exact lattice parameter for each sample, Nelson-Riley method was used. The Nelson-Riley function $F(\theta)$ is given as

$$F(\theta) = \frac{1}{2} \left[\left(\frac{\cos^2 \theta}{\sin \theta} \right) + \left(\frac{\cos^2 \theta}{\theta} \right) \right] \quad (3.4)$$

The values of all peaks is plotted against $F(\theta)$ of a sample. Using least square fit method, the lattice parameter a_0 is determined. The point where the least square fit straight line cut the y-axis is the actual lattice parameter of the samples.

3.7.2. Bulk Density Measurements

The physical or bulk density of the samples were determined by the formula,

$$\rho_B = \frac{M}{V} \quad (3.5)$$

Where ρ_B is the bulk density, M is the weight of the sample and V is the volume. V was determined by calculating the radius and thickness of the pellet and then put into the formula,

$$V = \pi r^2 h$$

The theoretical density is calculated by using the following expression,

$$\rho_{th} = \frac{8M}{N_A a_o^3} \text{ g/cm}^3 \quad (3.6)$$

Where n is the Avogadro number ($6.02 \times 10^{23} \text{ mol}^{-1}$), m is the molecular weight. Porosity was calculated from the relation,

$$\left\{ 100(\rho_{th} - \rho_B) / \rho_{th} \right\} \% \quad (3.7)$$

3.7.3. Study of Microstructure

Microstructure of the ferrite composition shows the grain size of the sample which is sintered at 1100°C. The samples were observed under high resolution optical microscope and photographed. Grain diameters were determined by liner intercept technique for which several random horizontal and vertical lines were drawn on the micrographs. Therefore the number of grains were counted that intersected and measured the length of the grains along the line traversed. Finally the grain size was calculated.

3.7.4. Complex Permeability Measurement

Permeability is a quantity that defines the change in self-inductance of a coil in the presence of a magnetic core. The core is taken as a toroid shape to avoid demagnetizing effects.

Complex initial permeability is given by

$$Z = R + jX = j\omega L_0 \mu = j\omega L_0 (\mu' - j\mu'')$$

Where the resistive part is,

$$R = \omega L_0 \mu''$$

And the reactive part is,

$$X = \omega L_0 \mu'$$

Here, L_0 is the inductance of the winding coil in air that is without loss.

μ is the permeability of the magnetic core

On the above expressions, the real part and the imaginary part were calculated by $\mu_i' = L_s/L_0$ and $\mu_i'' = \mu_i' \tan \delta$, where L_s is the self-inductance of the sample core sample core and $L_0 = \mu_o N^2 S / \pi \bar{d}$ derived geometrically.

N is the number of turns of the coil ($N = 4$), S is the area of cross section of the toroidal sample as given below:

$$S = d \times h,$$

Where $d = \frac{d_2 - d_1}{2},$

$$d_1 = \text{Inner diameter},$$

$$d_2 = \text{Outer diameter},$$

$$h = \text{Height}$$

And \bar{d} is the mean diameter of the toroidal sample as given below:

$$\bar{d} = \frac{d_1 + d_2}{2}$$

The relative quality factor is determined from the ratio $\frac{\mu_i'}{\tan \delta}$.

CHAPTER 4

Results and Discussion

4.1. X-Ray Diffraction Analysis

X-ray diffraction was done on $Li_xCu_{0.5}Zn_{0.5-2x}Fe_{2+x}O_4$ (with $x=0.00, 0.05, 0.10$) that were sintered at $1000\text{ }^{\circ}\text{C}$ in air for 5 hours to explore the spinel structure and physical properties of the samples. The results found in the experiment indicated that these materials have formed a well-defined single crystalline phase and formation of spinel structure for each composition. The positions of the peaks matched with the reported value [25]. In fig 4.1, X-ray patterns are shown for different compositions.

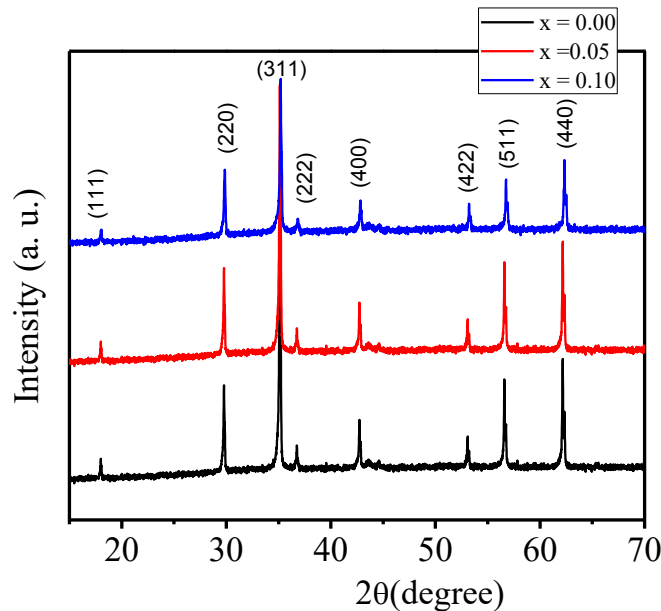


Fig 4.1: X-ray diffraction patterns for $Li_xCu_{0.5}Zn_{0.5-2x}Fe_{2+x}O_4$

From the XRD report, lattice parameter is found with the help of Nelson-Riley function. In fig 4.2, the lattice parameter is shown as a function of Li^+ content.

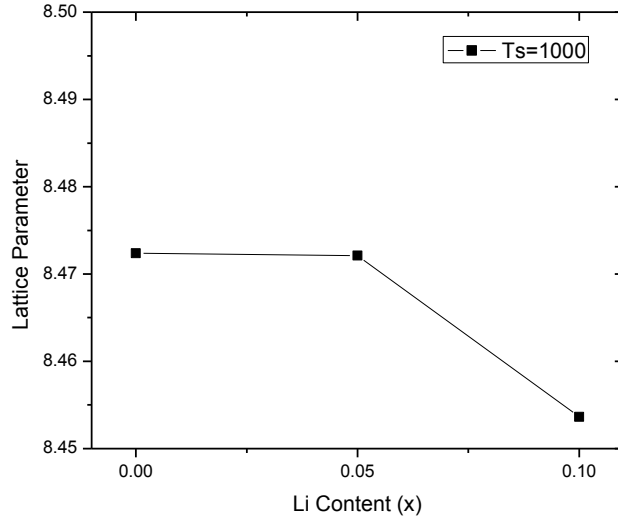


Fig 4.2: The variation of lattice parameter with Li^+ for $Li_xCu_{0.5}Zn_{0.5-2x}Fe_{2+x}O_4$

The lattice parameter decreases with Li^+ content which can be explained in terms of ionic radii. Li^+ has an ionic radius of (0.70 Å) and Fe^{3+} (0.78) both replaces Zn^{2+} (0.83 Å) [27]. Here big cations are getting replaced by small cations for which the lattice parameter has decreased. Both Li^+ and Fe^{3+} has smaller radius than Zn^{2+}

4.2. Bulk Density and Porosity

Bulk density, theoretical density and porosity for various compositions of $Li_xCu_{0.5}Zn_{0.5-2x}Fe_{2+x}O_4$ ($x=0.00$, $x=0.05$, $x=0.10$) are sintered at 950°, 1000°, 1050° and 1100°C have been calculated using the Eq-3.5, Eq-3.6, and Eq-3.7 respectively. The following fig 4.3 shows the variation of theoretical density and bulk density with increasing content of Li^+ at sintering temperature of 1000°C. It is possible to explain this phenomenon in terms of the

atomic weight of the constituents. The atomic weight of Zn (65.38 amu) is greater than atomic weight of the Li (6.941 amu) and Fe (55.845 amu) [28,29,32]. The increase of Li and Fe-content reduces the Zn-content, hence the total mass of the samples also reduces. As a result, the bulk density has decreased. Theoretical density depends on the lattice constant and molecular mass of the samples.

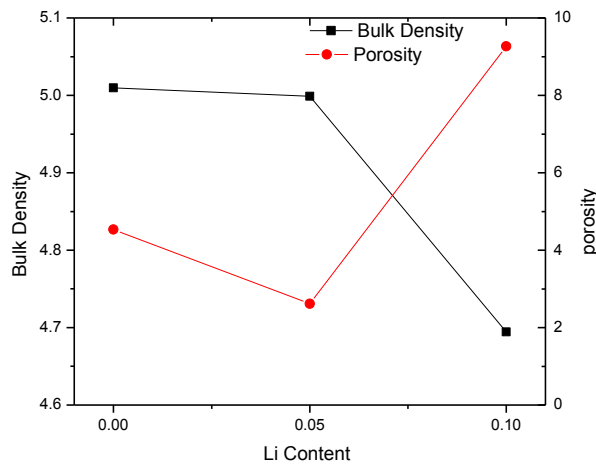
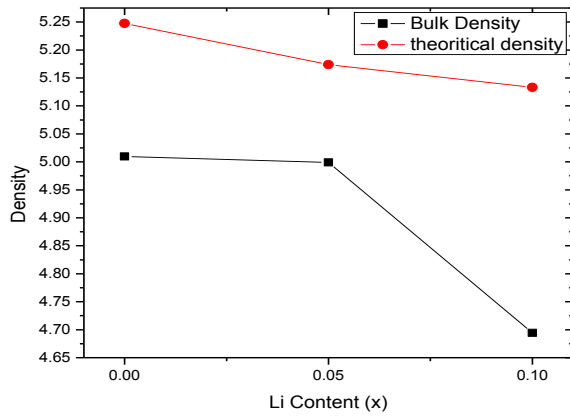


Fig 4.3: The variation of (a) Bulk and theoretical density sintered at 1000⁰C and (b) : Bulk density and porosity with Mn content for Li_x sintered at 1000⁰C

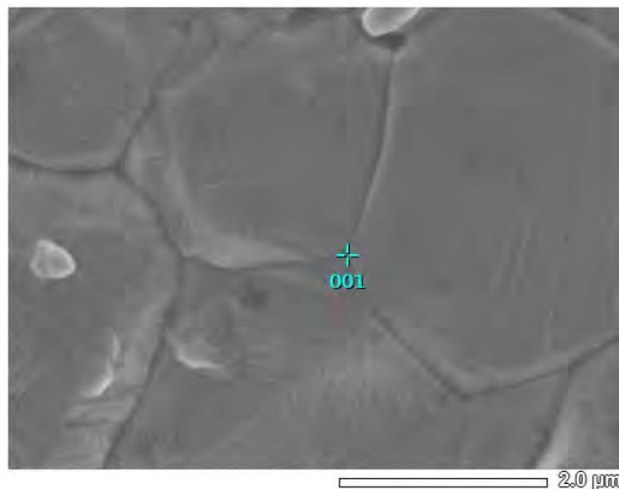
It is evident that the theoretical densities are larger on every point than their corresponding bulk densities which may be due to pores in the samples. Another trend can be identified from the same graph which shows the theoretical density has also decreased with the lattice parameter (a_0). This may be caused by Li^+ doping for which the total molecular mass lessened with increasing Li^+ content. Similar behavior is observed by Hamid [39].

4.3. EDS

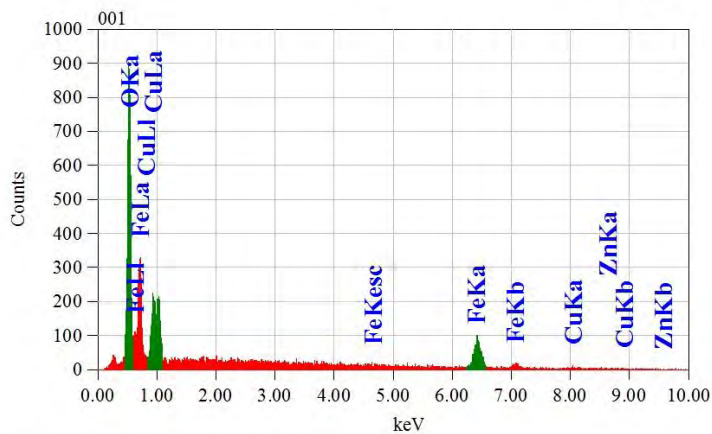
The purity and chemical composition of samples were checked using EDS analysis. Figure 4.7 and 4.8 show disparate surface points in EDS spectrum of the samples with $x=0.00$, $x=0.05$ and $x=0.10$ to conclude the homogeneity of the investigated samples. The concentrations of different constituents involved in the investigated sample at 10 KeV over various points on the surface of $Li_xCu_{0.5}Zn_{0.5-2x}Fe_{2+x}O_4$ with increasing Li^+ content are given in table 4.2. This table indicates the concentrations of different constituents are close to each other. The spectrum images reveal no trace of impurity and molar proportions of the present elements are in good agreement with that of expected values which shows there is no chemical reaction or any loss of ingredients.

View000

JEOLUSER 1/1



Title : IMG1
 Instrument : 7600F
 Volt : 5.00 kV
 Mag. : x 20,000
 Date : 2018/11/06
 Pixel : 512 x 384



Acquisition Parameter
 Instrument : 7600F
 Acc. Voltage : 10.0 kV
 Probe Current : 1.00000 nA
 PHA mode : T3
 Real Time : 30.21 sec
 Live Time : 30.00 sec
 Dead Time : 0 %
 Counting Rate : 777 cps
 Energy Range : 0 - 20 keV

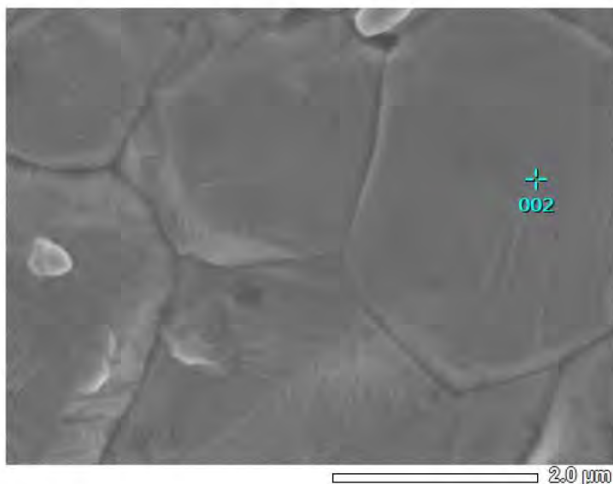
ZAF Method Standardless Quantitative Analysis
 Fitting Coefficient : 0.1071

Element	(keV)	Mass%	Sigma	Atom%	Compound	Mass%	Cation	K
O	0.525	29.72	0.14	60.50				38.9716
Fe	6.398	51.64	0.97	30.12				49.8074
Cu	0.930	6.85	0.18	3.51				6.1716
Zn	1.012	11.79	0.36	5.87				5.0494
Total		100.00		100.00				

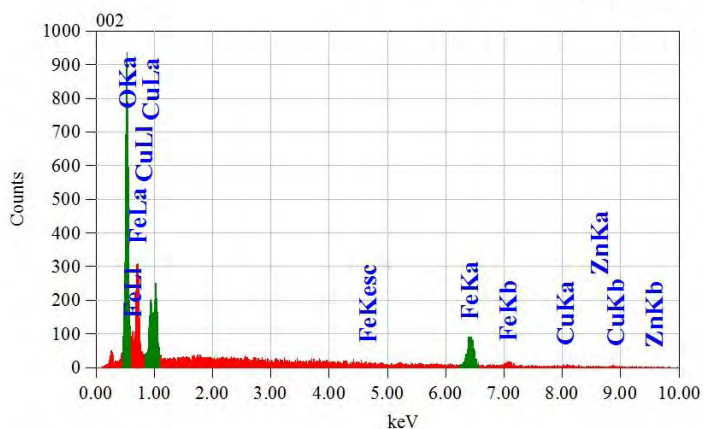
Fig 4.4: EDS pattern at point 1 for x=0.00

View000

JEOLUSER 1/1



Title : IMG1
 Instrument : 7600F
 Volt : 5.00 kV
 Mag. : x 20,000
 Date : 2018/11/06
 Pixel : 512 x 384



Acquisition Parameter
 Instrument : 7600F
 Acc. Voltage : 10.0 kV
 Probe Current: 1.00000 nA
 PHA mode : T3
 Real Time : 30.23 sec
 Live Time : 30.00 sec
 Dead Time : 0 %
 Counting Rate: 805 cps
 Energy Range : 0 - 20 keV

ZAF Method Standardless Quantitative Analysis
 Fitting Coefficient : 0.1216

Element	(keV)	Mass%	Sigma	Atom%	Compound	Mass%	Cation	K
O K	0.525	29.53	0.36	60.29				38.8357
Fe K	6.398	51.71	1.96	30.24				50.0806
Cu L	0.930	6.20	0.24	3.19				5.6428
Zn L	1.012	12.56	0.47	6.28				5.4409
Total		100.00		100.00				

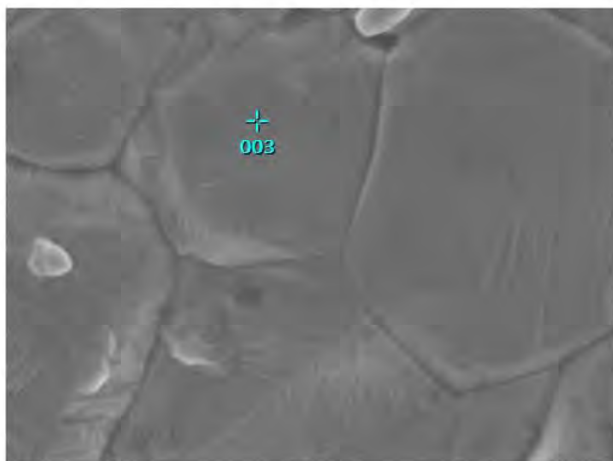
JED-2300 AnalysisStation

JEOL

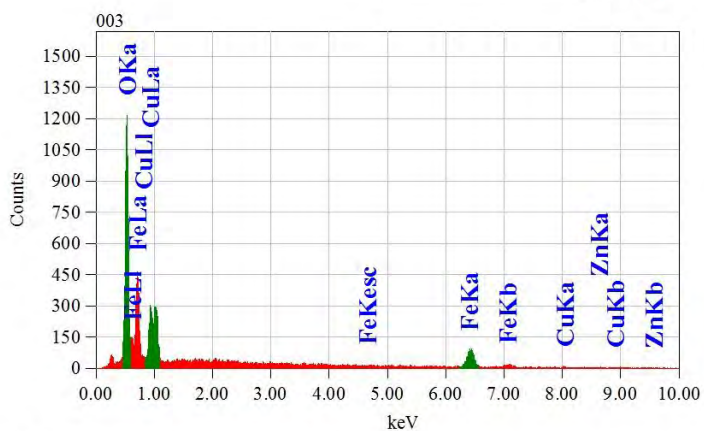
Fig 4.5: EDS pattern at point 2 for x=0.00

View000

JEOLUSER 1/1



Title : IMG1
 Instrument : 7600F
 Volt : 5.00 kV
 Mag. : x 20,000
 Date : 2018/11/06
 Pixel : 512 x 384



Acquisition Parameter
 Instrument : 7600F
 Acc. Voltage : 10.0 kV
 Probe Current: 1.00000 nA
 PHA mode : T3
 Real Time : 30.24 sec
 Live Time : 30.00 sec
 Dead Time : 0 %
 Counting Rate: 986 cps
 Energy Range : 0 - 20 keV

ZAF Method Standardless Quantitative Analysis

Fitting Coefficient : 0.1094

Element	(keV)	Mass%	Sigma	Atom%	Compound	Mass%	Cation	K
O K	0.525	33.44	0.14	64.73				43.6626
Fe K	6.398	44.77	0.84	24.83				42.9008
Cu L	0.930	7.97	0.17	3.89				7.3806
Zn L	1.012	13.83	0.34	6.55				6.0560
Total		100.00		100.00				

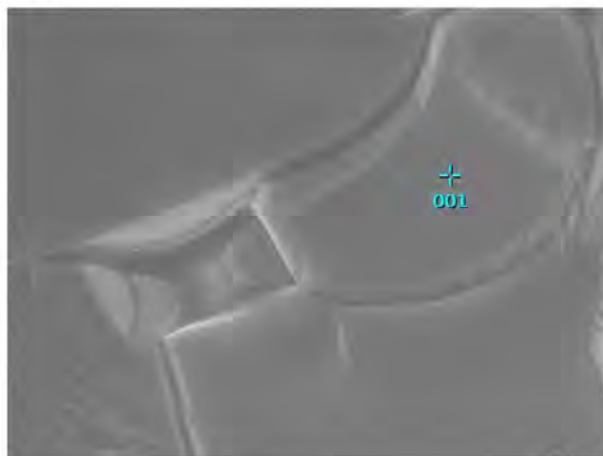
JED-2300 AnalysisStation

JEOL

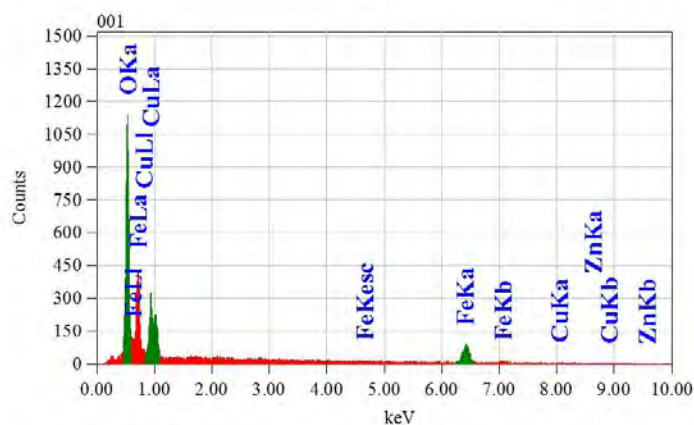
Fig 4.6: EDS pattern at point 3 for x=0.00

View000

JEOLUSER 1/1



Title : IMG1
 Instrument : 7600F
 Volt : 5.00 kV
 Mag. : x 20,000
 Date : 2018/11/06
 Pixel : 512 x 384



Acquisition Parameter
 Instrument : 7600F
 Acc. Voltage : 10.0 kV
 Probe Current: 1.00000 nA
 PHA mode : T3
 Real Time : 30.24 sec
 Live Time : 30.00 sec
 Dead Time : 0 %
 Counting Rate: 843 cps
 Energy Range : 0 - 20 keV

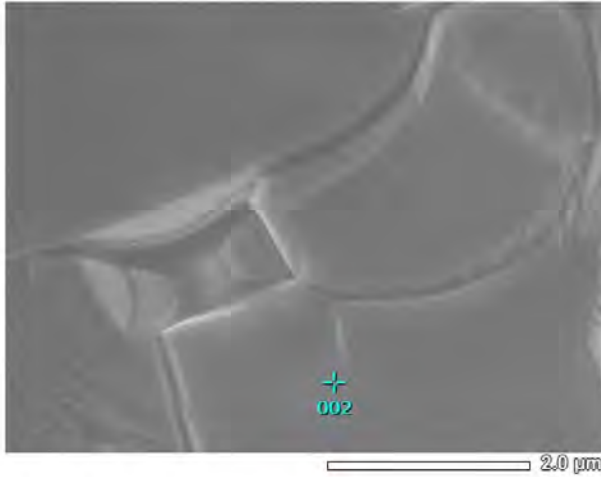
ZAF Method Standardless Quantitative Analysis
 Fitting Coefficient : 0.0845

Element	(keV)	Mass%	Sigma	Atom%	Compound	Mass%	Cation	K
O K	0.525	33.33	0.37	64.49				43.2214
Fe K	6.398	47.36	1.82	26.25				44.6862
Cu L	0.930	8.54	0.27	4.16				7.5708
Zn L	1.012	10.76	0.45	5.10				4.5216
Total		100.00		100.00				

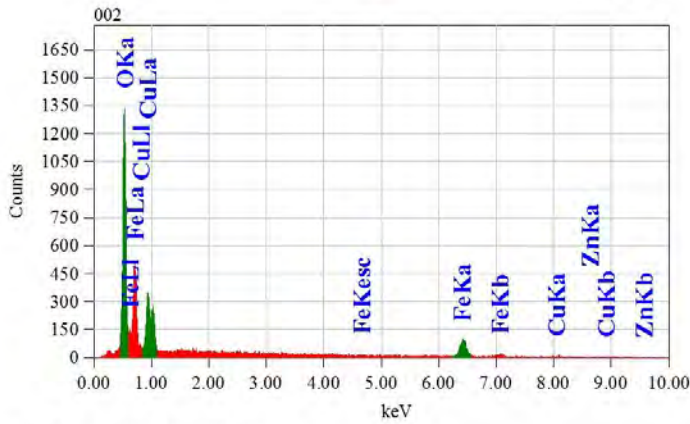
Fig 4.7: EDS pattern at point 1 for x=0.05

View000

JEOLUSER 1/1



Title : IMG1
 Instrument : 7600F
 Volt : 5.00 kV
 Mag. : x 20,000
 Date : 2018/11/06
 Pixel : 512 x 384



Acquisition Parameter
 Instrument : 7600F
 Acc. Voltage : 10.0 kV
 Probe Current : 1.00000 nA
 PHA mode : T3
 Real Time : 30.25 sec
 Live Time : 30.00 sec
 Dead Time : 0 %
 Counting Rate : 1030 cps
 Energy Range : 0 - 20 keV

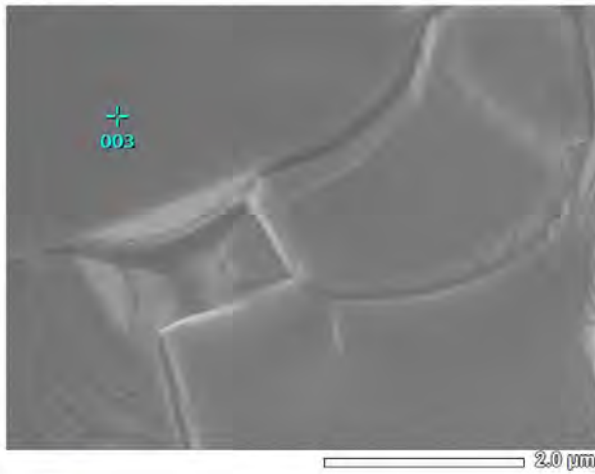
ZAF Method Standardless Quantitative Analysis
 Fitting Coefficient : 0.0921

Element	(keV)	Mass%	Sigma	Atom%	Compound	Mass%	Cation	K
O	0.525	34.88	0.13	66.12				45.1680
Fe	6.398	44.93	0.79	24.40				42.2378
Cu	0.930	8.54	0.17	4.08				7.6566
Zn	1.012	11.64	0.32	5.40				4.9376
Total		100.00		100.00				

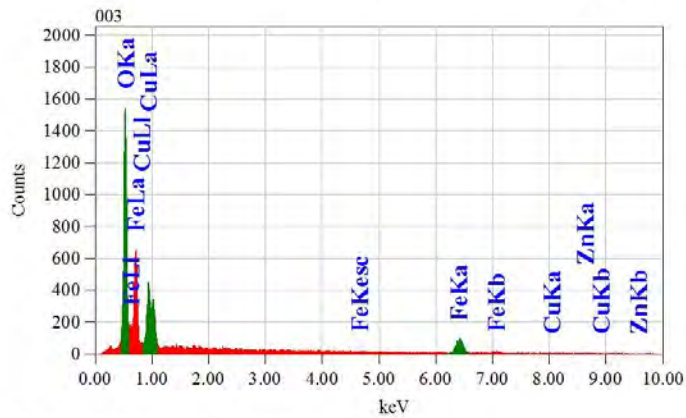
JED-2300 AnalysisStation

JEOL

Fig 4.8: EDS pattern at point 2 for x=0.05



Title : IMG1
 Instrument : 7600F
 Volt : 5.00 kV
 Mag. : x 20,000
 Date : 2018/11/06
 Pixel : 512 x 384



Acquisition Parameter
 Instrument : 7600F
 Acc. Voltage : 10.0 kV
 Probe Current : 1.00000 nA
 PHA mode : T3
 Real Time : 30.30 sec
 Live Time : 30.00 sec
 Dead Time : 1 %
 Counting Rate : 1195 cps
 Energy Range : 0 - 20 keV

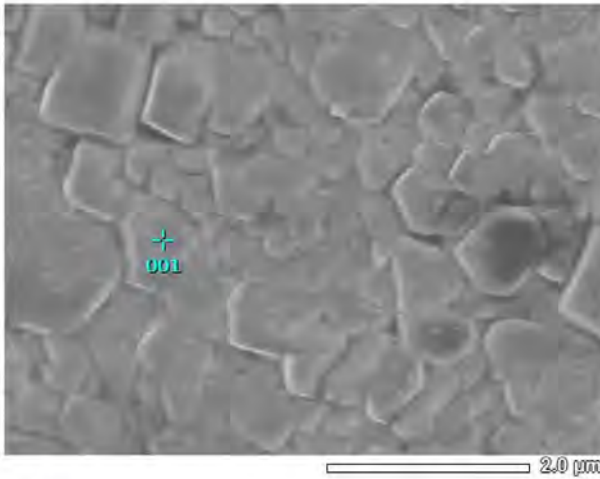
ZAF Method Standardless Quantitative Analysis
 Fitting Coefficient : 0.0818

Element	(keV)	Mass%	Sigma	Atom%	Compound	Mass%	Cation	K
O K	0.525	36.53	0.13	67.78				47.0883
Fe K	6.398	42.34	0.72	22.51				39.5121
Cu L	0.930	9.43	0.17	4.40				8.4494
Zn L	1.012	11.70	0.32	5.31				4.9502
Total		100.00		100.00				

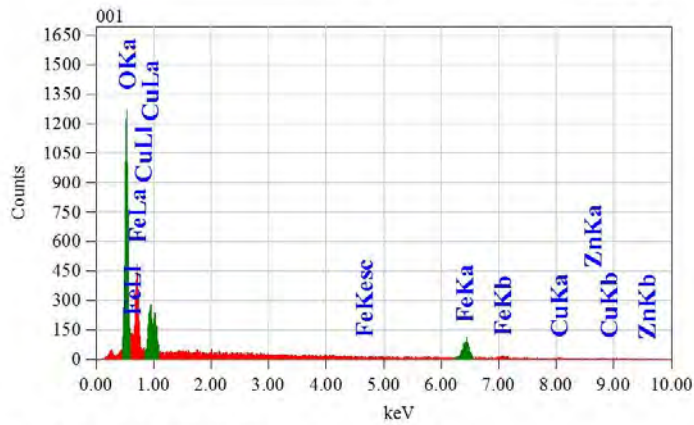
Fig 4.9: EDS pattern at point 3 for x=0.05

View000

JEOLUSER 1/1



Title : IMG1
 Instrument : 7600F
 Volt : 5.00 kV
 Mag. : x 20,000
 Date : 2018/11/06
 Pixel : 512 x 384



Acquisition Parameter
 Instrument : 7600F
 Acc. Voltage : 10.0 kV
 Probe Current: 1.00000 nA
 PHA mode : T3
 Real Time : 30.25 sec
 Live Time : 30.00 sec
 Dead Time : 0 %
 Counting Rate: 923 cps
 Energy Range : 0 - 20 keV

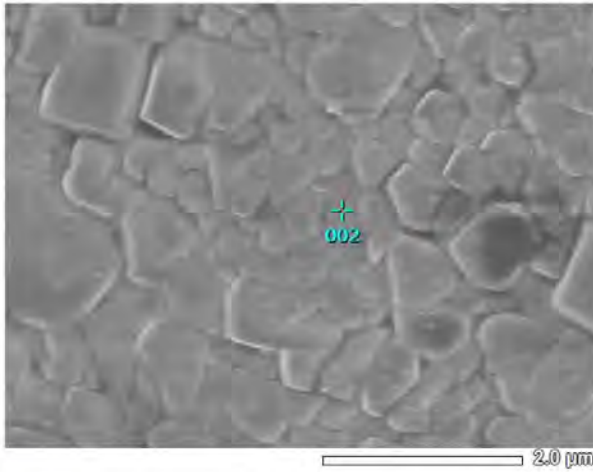
ZAF Method Standardless Quantitative Analysis

Fitting Coefficient : 0.1016

Element	(keV)	Mass%	Sigma	Atom%	Compound	Mass%	Cation	K
O	0.525	35.57	0.14	66.69				45.8577
Fe	6.398	46.57	0.87	25.01				43.1399
Cu	0.930	7.89	0.18	3.72				6.8795
Zn	1.012	9.96	0.33	4.57				4.1229
Total		100.00		100.00				

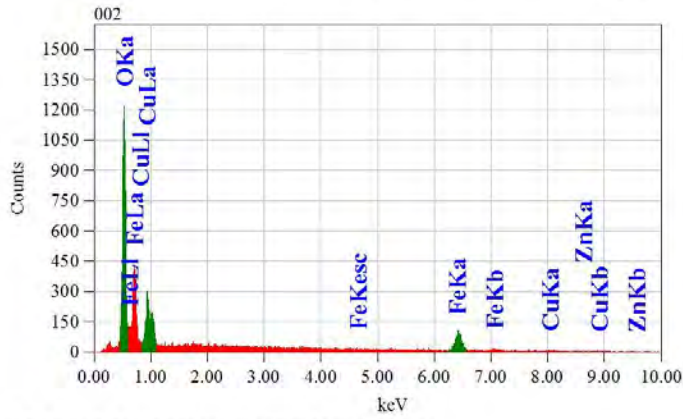
Fig 4.10: EDS pattern at point 1 for x=0.10

View000



JEOLUSER 1/1

Title : IMG1
 Instrument : 7600F
 Volt : 5.00 kV
 Mag. : x 20,000
 Date : 2018/11/06
 Pixel : 512 x 384



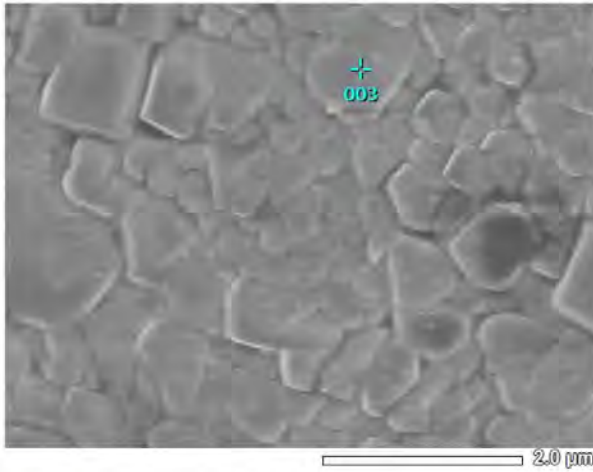
Acquisition Parameter
 Instrument : 7600F
 Acc. Voltage : 10.0 kV
 Probe Current : 1.00000 nA
 PHA mode : T3
 Real Time : 30.26 sec
 Live Time : 30.00 sec
 Dead Time : 0 %
 Counting Rate : 946 cps
 Energy Range : 0 - 20 keV

ZAF Method Standardless Quantitative Analysis
 Fitting Coefficient : 0.1058

Element	(keV)	Mass%	Sigma	Atom%	Compound	Mass%	Cation	K
O K	0.525	35.48	0.37	66.49				45.6102
Fe K	6.398	48.76	1.85	26.18				44.7376
Cu L	0.930	7.31	0.25	3.45				6.2239
Zn L	1.012	8.46	0.42	3.88				3.4283
Total		100.00		100.00				

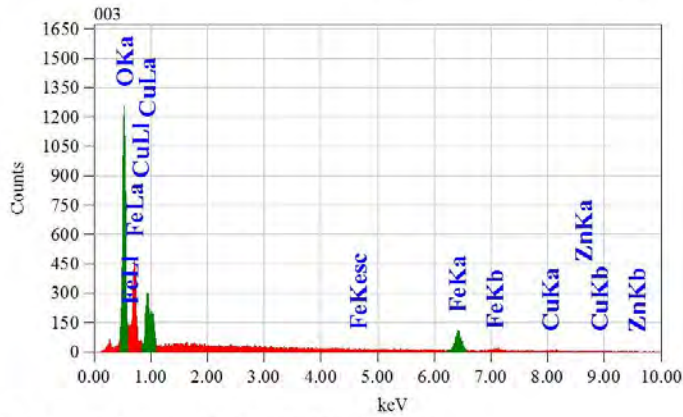
Fig 4.11: EDS pattern at point 2 for x=0.10

View000



JEOLUSER 1/1

Title : IMG1
 Instrument : 7600F
 Volt : 5.00 kV
 Mag. : x 20,000
 Date : 2018/11/06
 Pixel : 512 x 384



Acquisition Parameter
 Instrument : 7600F
 Acc. Voltage : 10.0 kV
 Probe Current : 1.00000 nA
 PHA mode : T3
 Real Time : 30.25 sec
 Live Time : 30.00 sec
 Dead Time : 0 %
 Counting Rate : 984 cps
 Energy Range : 0 - 20 keV

ZAF Method Standardless Quantitative Analysis
 Fitting Coefficient : 0.0999

Element	(keV)	Mass%	Sigma	Atom%	Compound	Mass%	Cation	K
O K	0.525	33.72	0.13	64.78				43.4960
Fe K	6.398	49.09	0.83	27.02				45.6925
Cu L	0.930	8.37	0.17	4.05				7.2077
Zn L	1.012	8.82	0.31	4.15				3.6039
Total		100.00		100.00				

JED-2300 AnalysisStation

JEOL

Fig 4.12: EDS pattern at point 3 for x=0.10

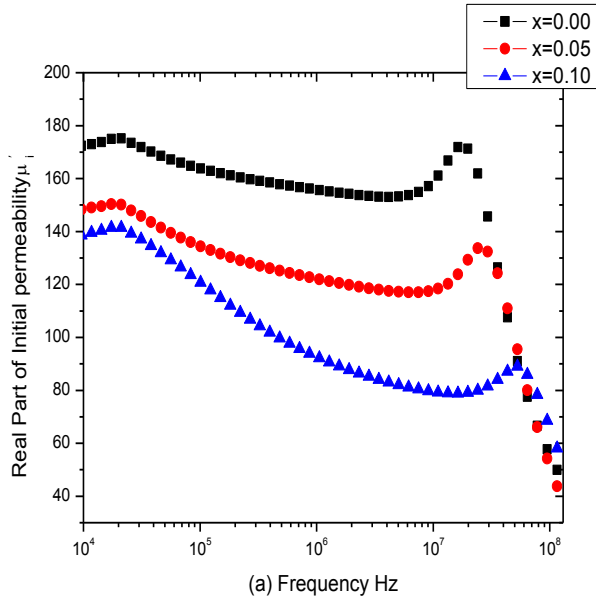
Table 4.1: Mass of different elements in various samples of $Li_xCu_{0.5}Zn_{0.5-2x}Fe_{2+x}O_4$ sintered at 1000°C

Composition	Elements	Point1 (%)	Point2 (%)	Point3 (%)	Expected (%)
$Cu_{0.5}Zn_{0.5}Fe_2O_4$	Cu	6.85	6.20	7.97	13.2304
	Zn	11.79	12.56	13.83	13.6123
	Fe	51.64	51.71	44.77	46.5083
	O	29.72	29.53	33.44	26.6489
$Li_{0.05}Cu_{0.5}Zn_{0.04}Fe_{2.05}O_4$	Cu	8.54	8.54	9.43	13.4400
	Zn	10.76	11.64	11.70	11.0624
	Fe	47.36	44.93	42.34	48.4264
	O	33.33	34.88	36.53	27.0712
$Li_{0.10}Cu_{0.5}Zn_{0.30}Fe_{2.10}O_4$	Cu	7.89	7.31	8.37	13.6565
	Zn	9.96	8.46	8.82	8.4304
	Fe	46.57	48.76	49.09	50.4062
	O	35.57	35.48	33.72	27.5070

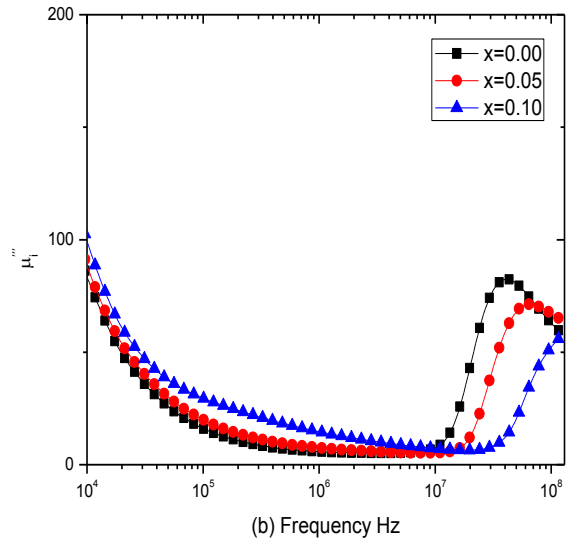
4.4. Complex Initial Permeability

The graphical analysis of complex permeability for various samples of $Li_xCu_{0.5}Zn_{0.5-2x}Fe_{2+x}O_4$ sintered at 950°, 1000°, 1050° and 1100°C have been shown in the fig 4.9, 4.10 and 4.11 respectively. The initial permeability (μ_i') decreases with increasing Li^+ content which is shown in figure 4.8. But at high frequency it becomes more stable with the increase of Li^+ content. It can be explained with the density. Permeability decreases with the decrease of density. The decrease in permeability with increase of Li^+ substitution can be attributed to the decrease in density. In figure 4.3 it is shown that the density decreases with the lithium content. This confirms that the origins of variation of the samples are due to the observed variation of microstructures and density as well [32].

The relative quality factor for various samples of $Li_xCu_{0.5}Zn_{0.5-2x}Fe_{2+x}O_4$ have been calculated from the loss factor for different sintering temperatures. This Q-factor is important for practical applications that indicate the measure of performance. Fig 4.10 shows the relative quality factor with increasing Li^+ content for 950°, 1000°, 1050° and 1100°C sintering temperatures. In figure 4.11, permeability and relative quality factor for different values of x with varying temperature is given. It is noticed that RQF is high for $Li_xCu_{0.5}Zn_{0.5-2x}Fe_{2+x}O_4$ in the absence of Li^+ at 950°C. At higher frequency, a sudden increase in permeability is noticed after a continuation of stability. This frequency is known as natural resonance frequency beyond which the permeability takes a sharp fall. This is common for all the values of x in every temperature.

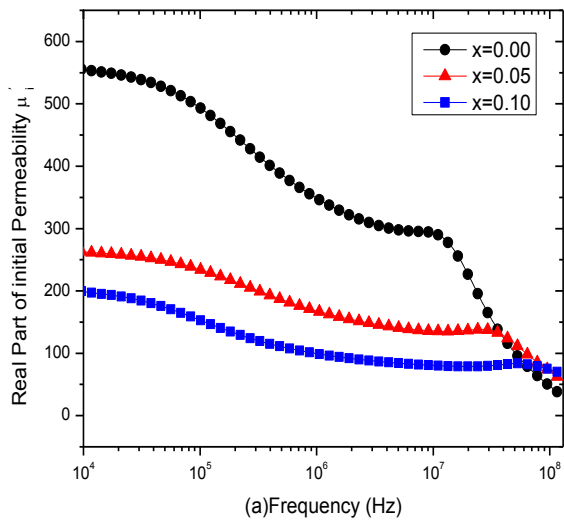


a) Real part of initial permeability

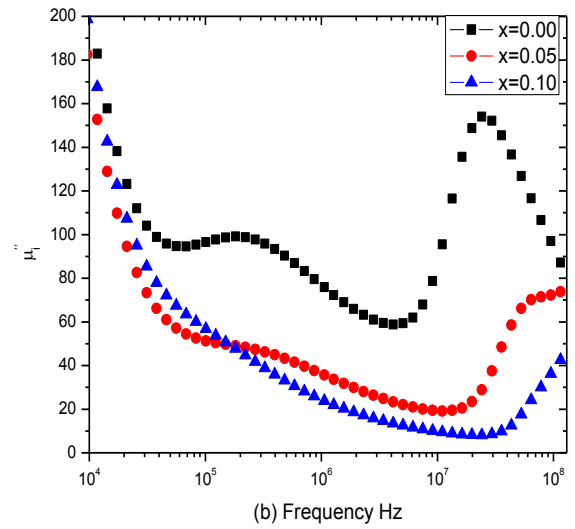


b) Imaginary part of initial permeability

Fig 4.13: At 950 °C

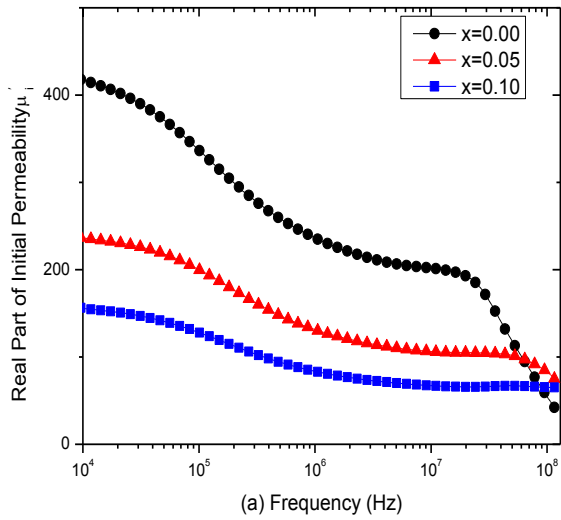


a) Real part of initial permeability

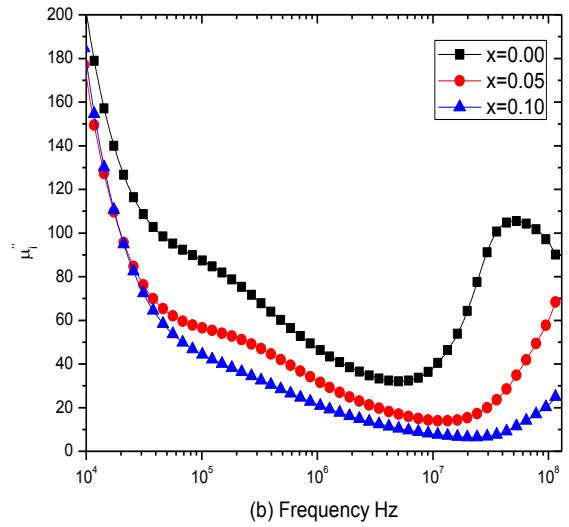


b) Imaginary part of initial permeability

Fig 4.14: At 1000 °C

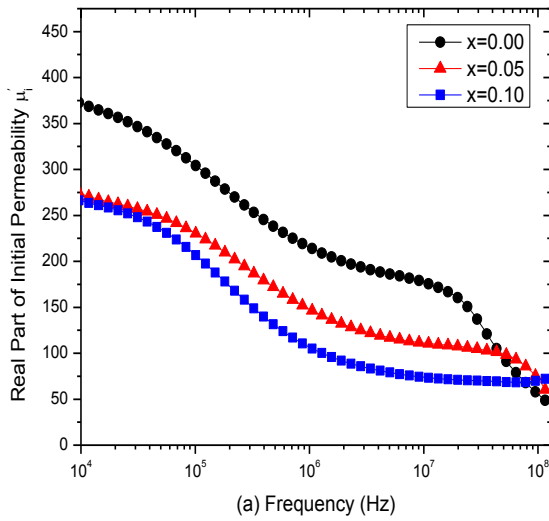


a) Real part of initial permeability

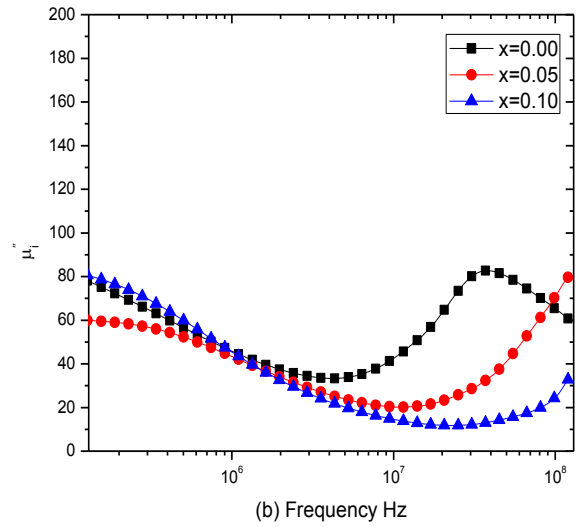


b) Imaginary part of initial permeability

Fig 4.15: At 1050 °C



a) Real part of initial permeability



b) Imaginary part of initial permeability

Fig 4.16: At 1100 °C

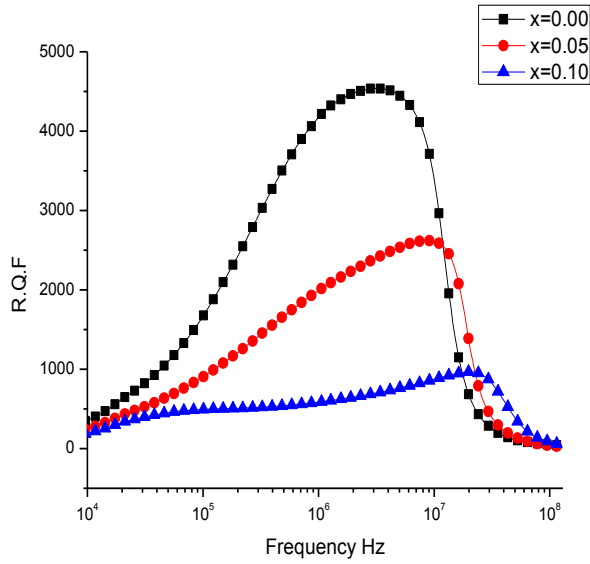


Fig 4.17: Relative Quality factor at 950°C

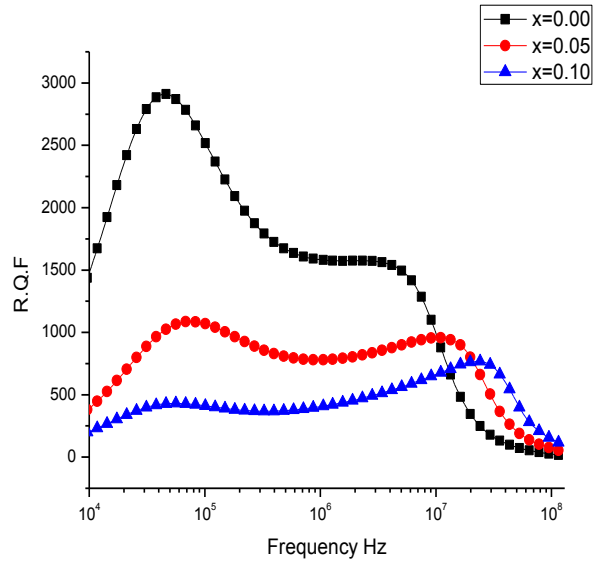


Fig 4.18: Relative Quality factor at 1000°C

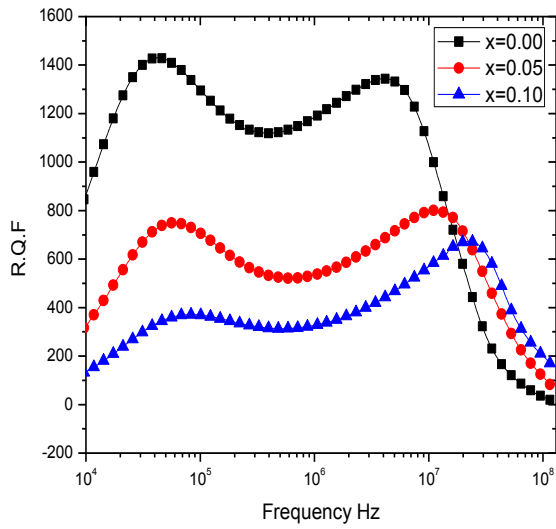


Fig 4.19: Relative Quality factor at 1050°C

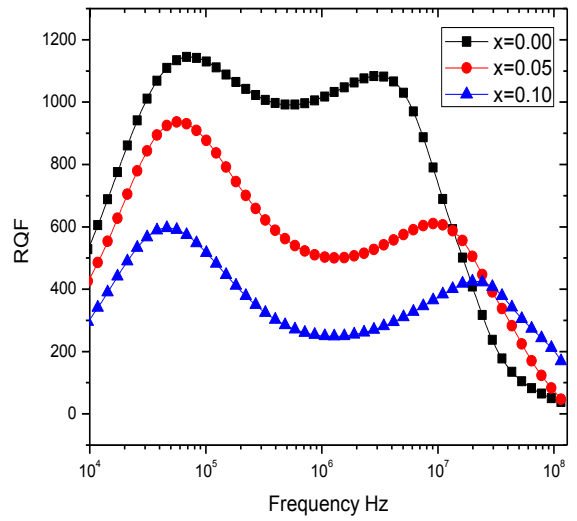
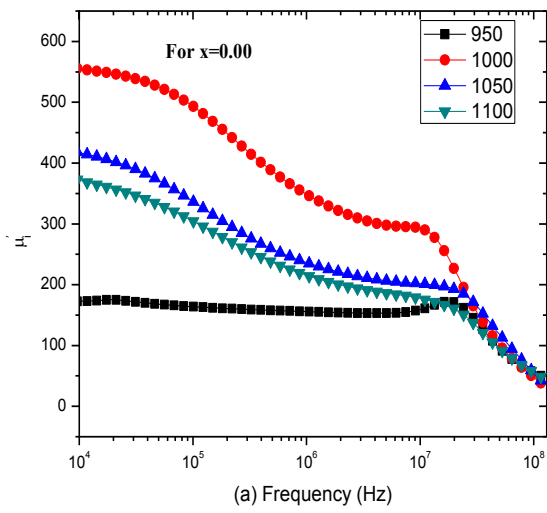
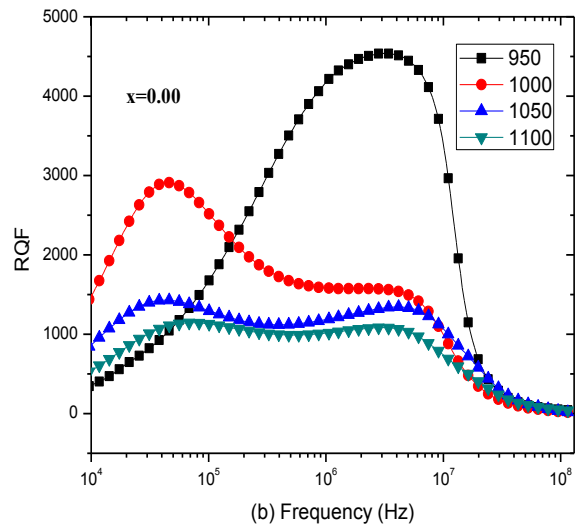


Fig 4.20: Relative Quality factor at 1100°C

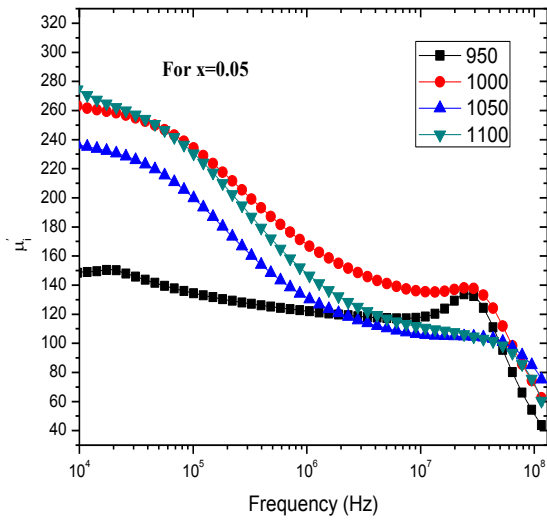


a) Permeability

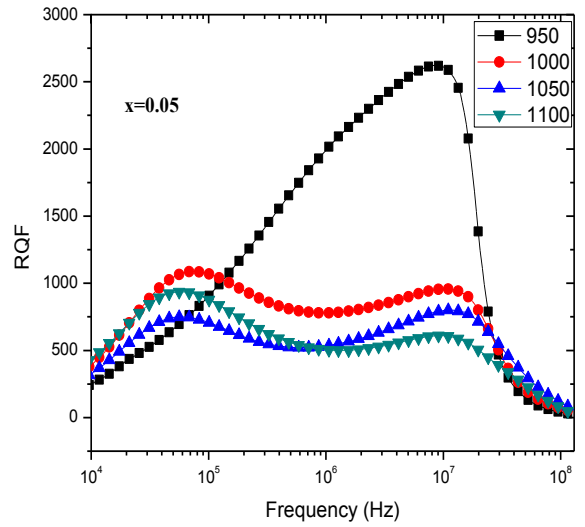


b) Relative quality factor

Fig 4.21: For $x=0.00$, at various temperatures

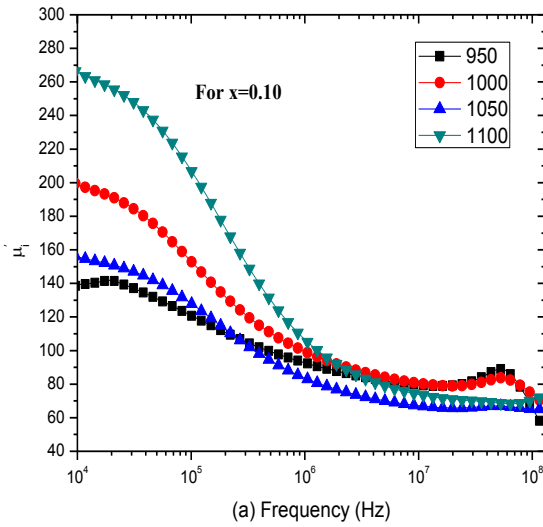


a) Permeability

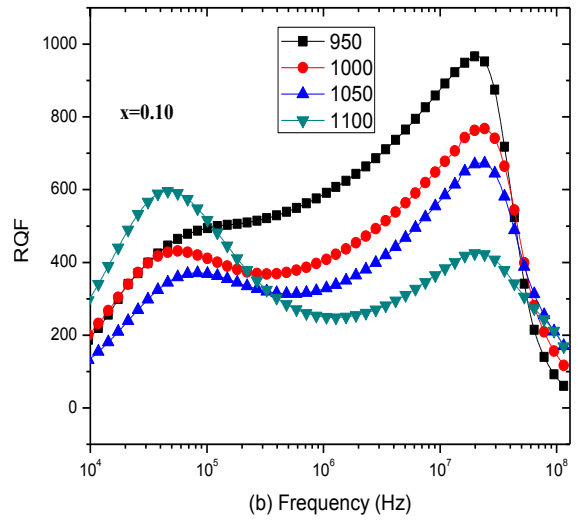


b) Relative quality factor

Fig 4.22: For $x=0.05$, at various temperatures



a) Permeability



b) Relative quality factor

Fig 4.23: For $x=0.10$, at various temperatures

4.5. Dielectric property:

Dielectric properties of the samples were measured for 1000° and 1050 °C. Dielectric constant (ϵ') of the samples were unstable in high frequency, it falls rapidly with the increase of frequency. More over with the increase of Li^+ content it decreases as well as shown in Fig 4.24 and Fig 4.25.

The variation of dielectric constant (ϵ') and loss with frequency is shown in Fig 4.24 and Fig 4.25. It can be seen from figure that the dielectric constant decrease and the loss at first increase and then decrease with increase of frequency. It indicates the usual dispersion behavior, which can be due to the Maxwell–Wagner type interfacial polarization in accordance with Koop's phenomenological theory [33–35].

The dielectric loss increases up to a certain frequency then it starts to fall and at higher frequency it reaches to a constant value. After a certain frequency ($> 10^4$) for $x=0.00$ it reaches to the maximum. The loss tangent decreases continuously with increase in frequency and attains a

constant value at higher frequencies. At higher frequencies domain wall motion is inhibited and magnetization changed by rotation and hence losses are found to be lower. As such, when the hopping frequency is nearly equal to that of the externally applied field, a maximum in loss tangent may be observed [36]. Similar results have been reported by Ku-mar et al. [32] in case of Li–Ti ferrites, and Ahmed et al. [37] in case of Ni-ferrites. Moreover, the substitution of Li^+ for Zn could modify the structural homogeneity which would cause a decrease in the degree of polarization [38].

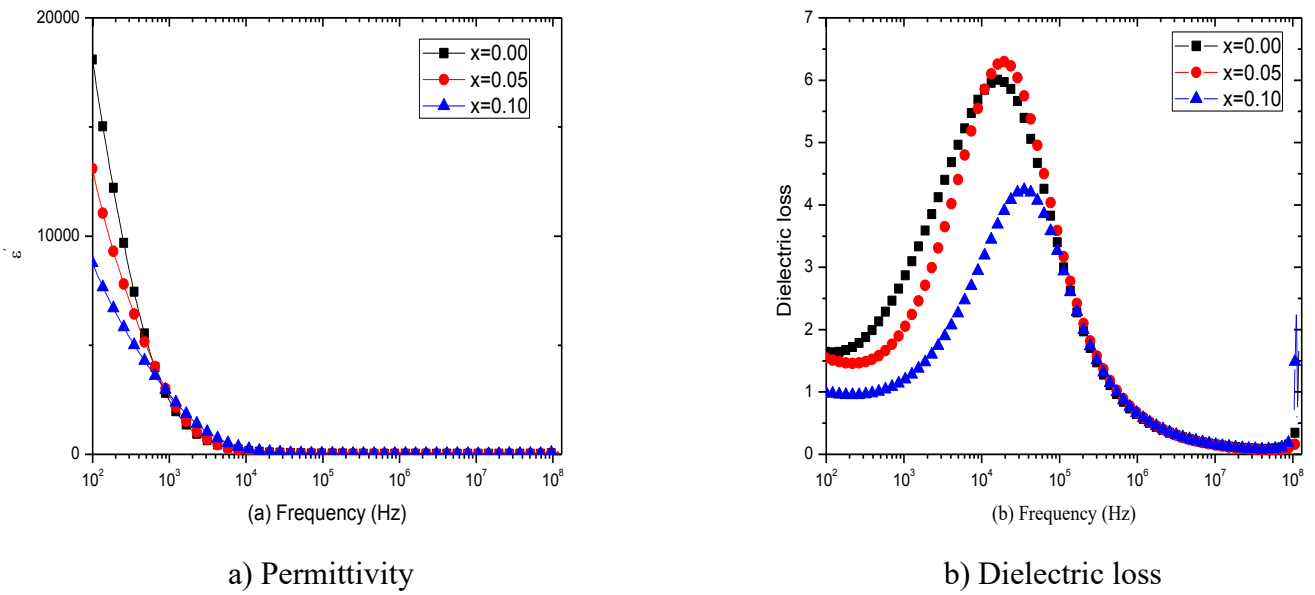
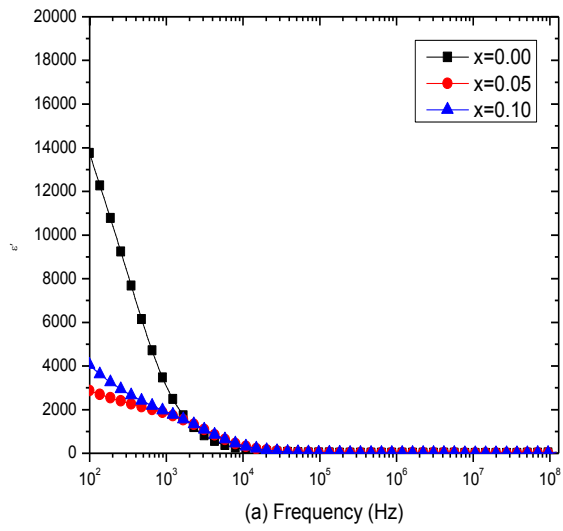
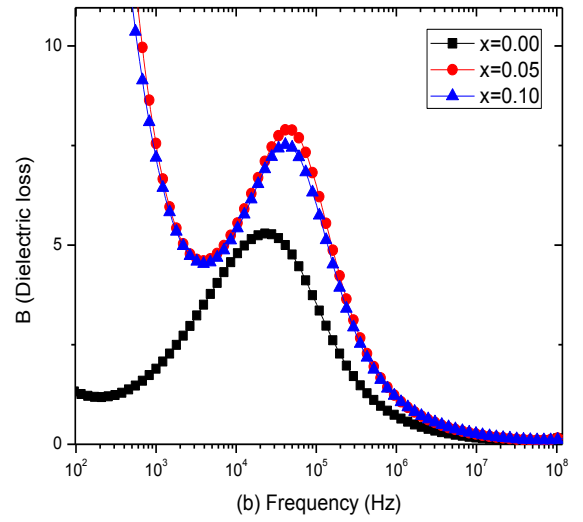


Fig 4.24: At 1000°C



a) Permittivity



b) Dielectric loss

Fig 4.25: At 1050°C

CHAPTER 5

Conclusions

Polycrystalline $Li_xCu_{0.5}Zn_{0.5-2x}Fe_{2+x}O_4$ ferrite is successfully prepared by solid state reaction method. The XRD patterns clearly indicate their single phase and formation of spinel structure. Lattice parameter a_0 decreases with increase of Li^+ content in $Li_xCu_{0.5}Zn_{0.5-2x}Fe_{2+x}O_4$. This is due to Li^+ has an ionic radius of 0.70 Å which replaces Zn^{2+} 0.83 Å. It is also observed that bulk density and theoretical density decreases with increasing porosity which may have resulted from the replacement of heavier elements Zn have atomic weight of 65.38(amu) with lighter element Li has atomic weight of 6.941 (amu). The EDS result shows the homogeneity of elements in the samples. The initial permeability (μ_i') decreases with increasing Li^+ content for temperature 950°, 1000°, 1050° and 1100° C. The general characteristic spectra of the real part remain constant in a certain frequency range, but then fall at higher frequencies to very small values. The resonant frequency f_r also increases with increasing Li^+ content. RQF value found to be the highest for $Li_xCu_{0.5}Zn_{0.5-2x}Fe_{2+x}O_4$ in the absence of Li^+ at 950°C.

Recommendations for Future Research

1. The number of samples could be increased for better understanding the relations and patterns.
2. Experiment could be done in lower sintering temperature around 950°C
3. Calcination temperature could be lower than 800°C
4. Temperature dependent permeability measurement could be done for further analysis.
5. Magnetization and SEM of each sample should have been done for better understanding the permeability spectra.

Reference

- [1] Rahman, M. M., Sonia, B. M., Das, M. K., Ahmed, F., Hossain, A., Saha, D. K., & Akhter, S. (2013). Structural and magnetization behaviors of Ni substituted Li-Mg ferrites. *International Journal of Physics*, 1(5), 128-132
- [2] Hossain, A. A., Rahman, M. A., Farhad, S. F. U., Vilquin, B., & Tanaka, H. (2011). Effect of Li substitution on the magnetic properties of $\text{Li}_x\text{Mg}_{0.40}\text{Ni}_{0.60-2x}\text{Fe}_{2+x}\text{O}_4$ ferrites. *Physica B: Condensed Matter*, 406(8), 1506-1511
- [3] Baba, P.D., Argentina, G., Courtney, W., Dionne, G. and Temme, D., 1972. Fabrication and properties of microwave lithium ferrites. *IEEE Transactions on Magnetics*, 8(1), pp.83-94.
- [4] Sabin, R. (2018). *U.S. Patent No. 9,854,807*. Washington, DC: U.S. Patent and Trademark Office.
- [5] Stijntjes, Theo & van Loon, Bob. *Early Investigations on Ferrite Magnetic Materials by J. L. Snoek and Colleagues of the Philips Research Laboratories Eindhoven*. 2008. Proceedings of the IEEE. 96. 900-904.
- [6] Dasan YK, Guan BH, Zahari MH and Chuan LK. ***Influence of La³⁺ Substitution on Structure, Morphology and Magnetic Properties of Nanocrystalline Ni-Zn Ferrite***. 2017. Available from: <https://doi.org/10.1371/journal.pone.0170075> [13th October 2017]
- [7] Singh A, Singh J, Disanjh HS. *Synthesis of Pure and Mixed Nickel-Cobalt Ferrites (Ni_{1-x}Co_xFe₂O₄) by Combustion Method and Characterization*. 2015. Available from: <http://www.jocpr.com/articles/synthesis-of-pure-and-mixed-nickelcobalt-ferrites-ni1xcoxfe2o4-bycombustion-method-and-characterization.pdf> [17th October 2017]
- [8] Rashid M, Kabir H, Rahaman M, Gafur A, Jamil ATMK and Ahmed SJ. *Investigation of Structural, Dielectric, and Electrical properties of Zn-substituted Li-Ni ferrite*. 2015. Available from: DOI : 10.9790/4861-07517683 [18th October 2017]

- [9] AdiChemistry. *Spinel and Inverse Spinel Structures*. Available from: <http://www.adichemistry.com/inorganic/cochem/spinels/spinel-structures.html> [20th October 2017]
- [10] Bland J. *CMP: Temperature Dependence*. 2003. Available from: <http://www.cmp.liv.ac.uk/frink/thesis/thesis/node40.html> [21st October 2017]
- [11] Kullabs. *Note on Classification of Magnetic Material*. Available from: <https://www.kullabs.com/classes/subjects/units/lessons/notes/note-detail/3067> [21st October 2017]
- [12] University of Birmingham. *Classification of Magnetic Materials*. Available from: <https://www.birmingham.ac.uk/Documents/college-eps/metallurgy/research/Magnetic-Materials-Background/Magnetic-Materials-Background-4-Classification-of-Magnetic-Materials.pdf> [21st October 2017]
- [13] Chikazumi S. *Physics of Magnetism*. 1964.
- [14] Hadfield D. *Permanent Magnets and Magnetism*. 1962.
- [15] Cullity BD. *Introduction to Magnetic Material*. 2009.
- [16] Sikder SS. *Temperature Dependence of Magnetization and Induced Magnetic Anisotropy of Some Fe, Co and Ni-based Amorphous Ribbons*. Ph. D. Thesis BUET Bangladesh. 1999.
- [17] Hussain KMA. *Study of Complex Permeability and Secondary Effects in Some Cobalt and Manganese Based Ferrites*. M. Phil. Thesis BUET Bangladesh. 2003.
- [18] Kittel C. *Introduction to Solid State Physics*, 7th edition, Jhon Wiley & Sons, Inc., Singapore. 1996.
- [19] Akther Hossain AKM, Seki M, Kawai T and Tabata H. *Colossal Magnetoresistance in Spinel type $Zn_{1-x}Ni_xFe_2O_4$* , *J. Appl. Phys.* 2004.
- [20] Goldman A. *Handbook of Modern Ferromagnetic Materials*, Kulwer Acad. Pub, Boston, U.S.A. 1999.

- [21] Valenzuela R. *Magnetic Ceramics*, Cambridge University Press, Cambridge. 1994.
- [22] Kingery WD, Bowen HK and Uhlman DR. *Introduction to Ceramics*, 2nd edition, Wiley Interscience, Newyork, pp. 476. 1976.
- [23] Coble RL and Burke JE. *4th Int. Symp. On the Reactivity of Solids*, Amsterdam, pp. 38-51. 1960.
- [24] I. McColm J and Clark M. *Forming, Shaping and Working of high Performance Ceramics*, Blackie, Glasgow, pp. 1-338. 1988.
- [25] Akhter Hossain AKM, Rahman ML. *Enhancement of Microstructure and Initial Permeability Due to Cu Substitution in $Ni_{0.50-x}Cu_xZn_{0.50}Fe_2O_4$ Ferrites*. 2011.
- [26] Adarakatti, S. N., Pattar, V. S., Korishettar, P. K., Grampurohit, B. V., Kharabe, R. G., Kulkarni, A. B., ... & Pujar, R. B. (2018). Synthesis, Structural and Electrical Studies of Li-Ni-Cu Nano Ferrites. *Acta Chemica Iasi*, 26(1), 1-12.
- [27] Jadhav, S. A. (2001). Magnetic properties of Zn-substituted Li-Cu ferrites. *Journal of Magnetism and Magnetic Materials*, 224(2), 167-172.
- [28] Quraishi, M. A. M., & Hossain, A. A. (2018, October). Study of the Structural and Magnetic Properties of Li Substituted Cu-Mn Mixed Ferrites. In *IOP Conference Series: Materials Science and Engineering* (Vol. 438, No. 1, p. 012013). IOP Publishing.
- [29] Akhter Hossain AKM, Rahman ML. *Enhancement of Microstructure and Initial Permeability Due to Cu Substitution in $Ni_{0.50-x}Cu_xZn_{0.50}Fe_2O_4$ Ferrites*. 2011.
- [30] https://www.electronics-notes.com/articles/basic_concepts/capacitance/dielectric-constant-relative-permittivity.php
- [31] https://en.wikipedia.org/wiki/Relative_permittivity
- [32] Parvin, R., Momin, A. A., & Hossain, A. A. (2016). Improvement of microstructure, initial permeability, magnetization and dielectric properties of nanocrystalline $LixCu_{0.1}Co_{0.1}Zn_{0.8-2x}Fe_{2+x}O_4$. *Journal of Magnetism and Magnetic Materials*, 401, 760-769.
- [33] Maxwell, J. C. (1881). *A treatise on electricity and magnetism*(Vol. 1). Clarendon press.

- [34] Wagner, K. W. (1913). KW Wagner, *Ann. Phys.* 40, 833 (1913). *Ann. Phys.*, 40, 833.
- [35] Koops, C. G. (1951). On the dispersion of resistivity and dielectric constant of some semiconductors at audiofrequencies. *Physical Review*, 83(1), 121.
- [36] Murthy, V. R. K., & Sobhanadri, J. (1976). Dielectric properties of some nickel-zinc ferrites at radio frequency. *physica status solidi (a)*, 36(2), K133-K135
- [37] Ahmed, M. A., El Nimr, M. K., Tawfik, A., & El Hasab, A. M. (1991). Dielectric behaviour in Ni-Al ferrites at low frequencies. *Journal of magnetism and magnetic materials*, 98(1-2), 33-36.
- [38] Ahmed, M. A., Mansour, S. F., & Afifi, M. (2012). Structural and electrical properties of nanometric Ni–Cu ferrites synthesized by citrate precursor method. *Journal of Magnetism and Magnetic Materials*, 324(1), 4-10.
- [39] Khan MHR, Akther Hossain AKM. *Reentrant Spin Glass Behavior and Large Initial Permeability of $Co_{0.5-x}Mn_xZn_{0.5}Fe_2O_4$* . 2012